

# SIFT Matching by Context Exposed

Fabio Bellavia

**Abstract**—This paper investigates how to step up local image descriptor matching by exploiting matching context information. Two main contexts are identified, originated respectively from the descriptor space and from the keypoint space. The former is generally used to design the actual matching strategy while the latter to filter matches according to the local spatial consistency. On this basis, a new matching strategy and a novel local spatial filter, named respectively blob matching and Delaunay Triangulation Matching (DTM) are devised. Blob matching provides a general matching framework by merging together several strategies, including pre-filtering as well as many-to-many and symmetric matching, enabling to achieve a global improvement upon each individual strategy. DTM alternates between Delaunay triangulation contractions and expansions to figure out and adjust keypoint neighborhood consistency. Experimental evaluation shows that DTM is comparable or better than the state-of-the-art in terms of matching accuracy and robustness, especially for non-planar scenes. Evaluation is carried out according to a new benchmark devised for analyzing the matching pipeline in terms of correct correspondences on both planar and non-planar scenes, including state-of-the-art methods as well as the common SIFT matching approach for reference. This evaluation can be of assistance for future research in this field.

**Index Terms**—Keypoint matching, SIFT, local image descriptors, local spatial filters, Delaunay triangulation, RANSAC, image context.

## 1 INTRODUCTION

KEYPOINT correspondences play a crucial role in many computer vision algorithms dealing with spatial localization. These include Structure from Motion (SfM) [1], image stitching [2], large-scale image retrieval [3] and Simultaneous Localization And Mapping (SLAM) [4], whose practical applications are more and more affecting everyday life in providing assistance or for mere entertainment. The emerging autonomous driving systems, together with the various applications of the augmented reality from medicine to gaming, represent some relevant examples in that sense.

This state of things has granted an active interest on this research topic over the decades, continuously evolving side by side with the novel advancements and challenges arising in the field. In this scenario, despite its age, the Scale Invariant Feature Transform (SIFT) [5], both as keypoint detector and as local image descriptor, is in good health. As a matter of fact, SIFT is still popular [6], [7] and generates descendants [8]–[11]. Moreover, SIFT has obtained satisfactory results in the last benchmarks [6], [7], [12] and recent applications still rely on it [13]. At the current state of the research, the keypoint extraction process and the computation of the associated local image descriptors, that must be synergically used to establishing correspondences, seem to have reached somewhat their limits when the matching process is considered untied from the context provided by the source images [14]. This observation is reflected in the progress done by deep learning descriptors [14]–[19] in conjunction with the availability of ever more big datasets [7], [20], [21]. In this paper two different matching context are discussed.

The first one is provided by the *descriptor space*. Mutual Nearest Neighbor (NN) and the Nearest Neighbor Ratio (NNR) [5], two of the most commonly employed matching strategies are examples of this context exploitation. NN requires a match to be the best on both the input pair images,

i.e. NN considers a *inter-relation* in the descriptor space. NNR selects matches according to the ratio between the first and second best distances inside the reference image, i.e. NNR considers a *intra-relation* in the descriptor space.

The other matching context is the one provided by the *keypoint space* over the images. This kind of scene knowledge includes patch relative orientations [11] and keypoint spatial relations [22]–[30], which have been exploited to successfully disambiguate matches, boosting the final matching accuracy. Model constraints such those imposed by planar scenes and epipolar geometry [31], mainly built upon the Random SAmples COnsensus (RANSAC) [32]–[37], also operate on the keypoint space and generally represent the final post-filtering step of the entire process. Although very effective, this last kind of model-based matching is somewhat less general since it is not valid in all situations, such as in the case of moving or deformable objects that violate the constraint of a single rigid structure [22].

The recent evolution of deep networks jointly training a keypoint detector and descriptor [38]–[42] has brought fresh attention to the matching step inherently correlated to scene context, as the next step to be included in an all-in-one deep matching network [14], [43]. In this paper existent and novel general matching strategies exploiting image context in terms of both descriptor and keypoint spaces are presented and discussed. As baseline, their applications to SIFT are considered, but results on other keypoint detectors and descriptors are also shown. The contributions of this study can be mainly divided into three typologies:

- Descriptor space context: Starting from a known greedy matching strategy using one-to-one NN together with NNR, several potential enhancements that include rank-based filtering as well as many-to-many and symmetric matches are investigated, extensively combined, and evaluated. The overall matching strategy obtained by merging altogether the best approaches, named blob matching, is proved

F. Bellavia is with the Department of Mathematics and Computer Science, Università degli Studi di Palermo, Via Archirafi, 34, 90123 Palermo, Italy, e-mail: name.surname@unipa.it .

to give more correct correspondences with respect to each individual matching strategy it is based upon.

- Keypoint space context: A new robust and effective local spatial filter named Delaunay Triangulation Matching (DTM) is designed. DTM associates matches greedily, according to the consistency of the keypoint spatial local neighborhoods. Neighborhood relations are obtained on the basis of Delaunay triangulations on the source images. DTM can guarantee comparable or better matching results with respect to the state-of-the-art.
- Benchmarking image matching by context: A new evaluation aimed at comparing state-of-the-art spatial matching strategies is devised, evaluating their behaviors on different keypoint detectors and very recent descriptors on both planar and non-planar scenes. In this latter case, ground-truth correct matches are checked according to [6]. With respect to other evaluations merely relying on the epipolar distance [44], this setup avoid incorrect associations due to epipolar ambiguity and, differently from benchmarks based on camera pose estimation error [7], provides direct evaluation scores.

The rest of the paper is organized as follows: Related work is presented in Sec. 2, blob matching is defined in Sec. 3, DTM in Sec. 4, and proposed benchmark setup and results are discussed in Sec. 5. Finally, conclusions and future work are outlined in Sec. 6.

## 2 RELATED WORK

Assigning correspondences requires the close cooperation between three main subjects: The keypoint detector, the local image descriptor and the matching strategy.

A good keypoint detector for this task must be able to extract distinctive yet repeatable characteristic points on the input images. Moreover, the number of detected keypoints should be sufficient to provide a good coverage of relevant structures of the scene but, at the same times, the number of keypoints should be limited so as to make the computational process feasible and to reduce the chance of false matches. Keypoint distinctiveness decreases as the number of detected keypoints increases, especially in the presence of repeated structures on the image. Classical keypoint detectors usually extract corners or blob-like structures. Corner detectors are mainly based on the autocorrelation matrix [45], while blob detectors may employ the Hessian matrix, the Laplacian of Gaussian (LoG) [46] or the Difference of Gaussian (DoG) [5]. Scale and affine adaptations [46] can be exploited to improve the repeatability. Fast keypoint detectors can be devised by box filter approximations [47] or by employing local intensity tests [48], [49], where the best test sequences can be extrapolated by machine learning [49]. Recently, keypoint detectors based on deep learning have started to emerge, especially in frameworks where detectors and descriptors sharing a common network are jointly estimated [38]–[42], or by combining handcrafted and deep learned filters [50]. Experimental evaluation in Sec. 5 will be carried out considering the state-of-the art SIFT and the HarrisZ detector [51]. SIFT is a well known blob-like DoG multi-scale detector, while HarrisZ is an affine multi-scale

corner detector. Relying on Harris corners, HarrisZ uses an adaptive filter response to select keypoints and a scale-based noise filtering that produces effects similar to the non-linear scales-space extraction of [52].

Local image descriptors are used to obtain a meaningful numerical vector encoding the distinctive attributes of a keypoint patch, i.e. the local keypoint neighborhood. Ideally, descriptors for the same keypoint undergoing both geometrical or color distortions must be close in the descriptor vector space, and the opposite must hold for distinct keypoints. A trade-off between the descriptor tolerance to image deformation and its discriminability is often required, since high descriptor invariance decreases descriptor discriminability. Local image descriptors can be divided into hand-crafted and data-driven descriptors. Handcrafted descriptors are mainly expressed in terms of gradient orientation histograms [5], [11], [53], pixel ordering [54], Haar wavelets [47], kernel convolutions [55] or binary intensity comparisons [48], [49]. Data-driven descriptors are instead defined and finely tuned according to the image context, provided in terms of input training data, in order to obtain low-dimensional descriptors while optimizing the accuracy of the matching process [9], [49], [56]. Gradient orientation histogram descriptors include SIFT and its extensions [8], [10], [11], [57], also as data-driven descriptors [9], [56]. Among data-driven descriptors, deep descriptors have recently shown to outperform any other descriptor [6], [7], [12] thanks to the modern hardware capability offered by GPUs and the availability of large training datasets [7], [21]. Triplet loss [15], [16], hard negative mining [17], second-order similarity [19], geometric constraint integration [18] and jointly detector-descriptor optimization [14], [41], [42] are some of the techniques employed to get state-of-the-art results. On one hand, matching strategy evaluation carried out in Sec. 5 will employs the handcrafted descriptors RootSIFT [8] and the double square-rooting shifting Gradient Local Orientation Histogram (RootsGLOH2) [58]. On the other hand, the deep Second Order Similarity Network (SOSNet) [19] and HardNet2 [59] will be used. RootSIFT improves upon SIFT by replacing the Euclidean distance with the Hellinger's distance. In addition to RootSIFT, RootsGLOH2 provides a mechanism to better handle patch orientation estimation. Deep-based SOSNet and HardNet2 are the current state-of-the-art, while RootsGLOH2 has been shown to be actually the current best handcrafted descriptor [58].

Patch normalization is the interface between keypoint extraction and local descriptor computation, and it is often addressed together with this last step. The most common patch normalization approach is that of SIFT, yet other approaches exists [47], [49], [60]. In particular, it has been reported in [6], [53] that orientation estimation is one the most critical aspect that needs to be handled. The deep patch orientation assignment designed in [61] was proved to improve the matching accuracy noticeably [6] and will be employed for the evaluation presented in Sec. 5.

Matches are assigned by pairwise inspecting descriptor similarity in the descriptor space and optionally by considering keypoint displacement in the images. The most common pipeline uses mutual NN or NNR matching followed by RANSAC. Using symmetric NNR [6] or considering the first geometrical inconsistent match in NNR [62]

have been demonstrated to generally improve the matching process. Further improvements have been observed when considering many-to-many putative matches instead of constraining matches to be only one-to-one [63]. This fact can be linked back to the strategy of employing multiple synthesized views to enrich the matches in Affine SIFT (ASIFT) [64]. Moreover, simple spatial heuristics such as the topological filter [65] or displacement constraints according to motion hypothesis [66] can be effective to reduce false correspondences, even if RANSAC remains the best choice until now. The simple original RANSAC implementation has been extended in several ways to raise its accuracy and speed, exploiting both feature and keypoint space contexts. PROgressive SAmple Consensus (PROSAC) [33] sampling is guided by the degree of similarity between the matched descriptors, while Spatially Consistent RAndoM SAmple Consensus (SCRAMSAC) [34] pre-filters the candidate samples according to their local neighborhood in the keypoint space, and the recent Graph-Cut RANSAC [36] considers the spatial coherence between models. The Universal framework for RANSAC (USAC) [35] implements many of the less recent RANSAC extensions altogether. Although quite powerful, robust model regression strategies like RANSAC and its extensions, or similar approaches [67], can be limiting when violating the assumption of rigid scenes such as in the case of moving and deformable objects, unless handling multiple models [68]. In order to go beyond this limitation, several strategies have been proposed for filtering correspondences relying on the spatial local neighborhood of the keypoints. Vector Field Consensus (VFC) [26] estimates a smooth optical flow, COherence based DECision boundaries (CODE) [28] exploits non-linear optimization to model motion, Locality Preserving Matching (LPM) [22] iteratively removes highly inconsistent matches, Grid-based Motion Statistics (GMS) [23] filters matches according to the local neighborhood consistency upon a grid subdivision, and Learning for Mismatch Removal (LMR) [24] uses local neighborhood relations to learn how to classify matches. In addition, the locally linear transforming (LTT) is defined in [27] for the same aim and, more recently, clustering techniques [29] and combinations of previous approaches [30] have also been investigated. Starting with PointCN [69], deep networks have been recently developed to assign correspondences as well. PointNet exploits context normalization to encode global image context, while Order-Aware Network (OANet) [70] relies on new pooling layers to extract complex local and global image contexts. SuperGlue [43] leverages the concepts of self and cross attentions, and in Neural-Guided RANSAC (NG-Ransac) [37] model sampling is guided by deep learning. As last note, all these matching strategies can be used to pre-filter candidate matches to boost RANSAC in terms of both efficiency and accuracy. When feasible, executing RANSAC after any other kind of match selection is always the best practice.

### 3 BLOB MATCHING

Blob matching mainly works by filtering matches through descriptor space context heuristics. Before defining the blob matching, the base matching strategies it relies upon are reviewed and discussed. The notation adopted hereafter

assumes that  $D \in \mathcal{R}^{n \times m}$  is a matrix such that  $D_{ij}$  is the distance between the descriptors associated to the  $i$ -th keypoint on the first image  $I_1$  and the  $j$ -th keypoint on the second image  $I_2$ .  $D_{ijw}$  denotes the  $w$ -th lowest value entry found on row  $i$ , i.e. the  $w$ -th best descriptor association. Likewise,  $D_{iwj}$  is the  $w$ -th lowest value entry on column  $j$ , and the subscript  $\Downarrow$  denotes the extraction of the index pair  $(i, j)$  from  $D_{ij}$ , done element-wise in the case of sets of matches. NN is the basic way to associate correspondences

$$S_{NN} = \{D_{ij^1}\}_{\Downarrow} \quad (1)$$

Here, the index spans  $1 \leq i \leq n$  and  $1 \leq j \leq m$  are omitted for simplicity. Mutual NN constrains even more  $S_{NN}$  by requiring that selected matches must be the best in both the images, i.e. simultaneously on both D rows and columns

$$S_{mNN} = \{D_{ij^1} = D_{i^1j}\}_{\Downarrow\Downarrow} \quad (2)$$

It is easy to see that  $S_{mNN} \subseteq S_{NN}$ . NNR [5] considers instead a matrix  $D'$  such that

$$D'_{ij} = \frac{D_{ij}}{D_{ij^2}} \quad (3)$$

and the threshold  $t_r$ , usually set to 0.8, so that

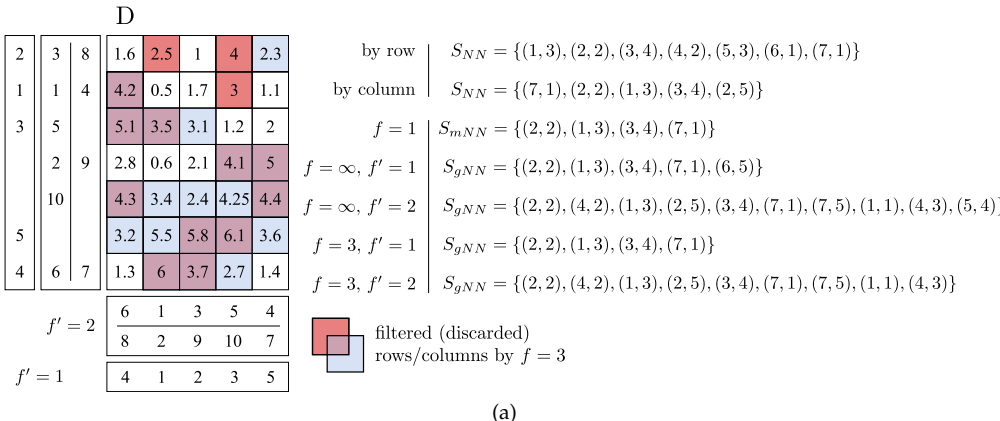
$$S_{NNR} = \{D'_{ij^1} \leq t_r\}_{\Downarrow\Downarrow} \quad (4)$$

NNR can be related to the triplet matching learning adopted by deep descriptors starting from [15]. Notice that  $D'_{ij} \in [0, 1]$  by definition, and  $D'_{ij^1\Downarrow} = D_{ij^1\Downarrow}$  for any row since scalar multiplication does not affect the ordering. NNR is usually more accurate than mutual NN since NNR relative values can better express the image context than NN absolute values. Nevertheless,  $S_{mNN}$  is symmetric since it takes both images as reference, and provides a one-to-one matching relation. By contrast,  $S_{NNR}$  considers only the first image  $I_1$  as reference, since the denominator in Eq. 2 is computed on rows, providing a one-to-many matching relation. In order to relax the strict requirements of mutual NN, the following greedy strategy, to the best of the author's knowledge first mentioned in [71], can be employed. As notation,  $D_k$  is the  $k$ -th best entry of the matrix  $D$  considered as linear vector and  $G$  is the set of matches, initially empty. At each iteration  $1 \leq k \leq r \times m$ ,  $D_k$  is added to  $G$  if both  $D_{k\Downarrow} \notin G_{\Downarrow}$  and  $D_{k\Downarrow} \notin G_{\Downarrow\Downarrow}$ , where the subscripts  $\Downarrow$  and  $\Downarrow\Downarrow$  denote the operators that extract the row and column index of the entry, respectively. The final matching set is

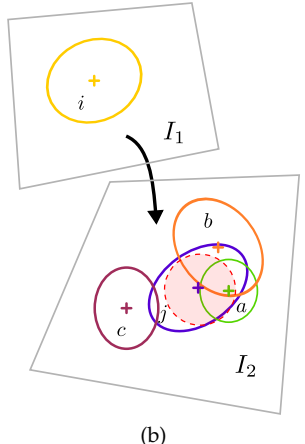
$$S_{gNN} = \{G\}_{\Downarrow\Downarrow} \quad (5)$$

Under the assumption that  $D$  entries have unique values, it holds that  $S_{mNN} \subseteq S_{gNN}$  and  $|S_{gNN}| = \min(n, m)$ . If a mutual match  $(i, j)$  of  $S_{mNN}$  has not been included in  $S_G$ , there would have been a match  $(\tilde{i}, \tilde{j})$  with  $i = \tilde{i}$  or  $j = \tilde{j}$  at some previous iteration such that  $D_{\tilde{i}\tilde{j}} < D_{ij}$ . This is a contradiction since  $D_{ij} = D_{i^1j} = D_{ij^1}$  by definition. Figure 1a shows the difference between  $S_{NN}$ ,  $S_{mNN}$  and  $S_{gNN}$ .

Mutual or greedy NN can be combined with NNR, in the sense that matches are extracted by NN but sorted and eventually filtered according to the NNR ranking. In this



(a)



(b)

Fig. 1. (a) Comparison of the different matching strategies discussed in the text. NN matching can be done row-wise or column-wise according to the input image selected as reference and cannot be obtained by blob matching. Default one-to-one  $S_{mNN}$  can be obtained by setting  $f = 1$ , while  $S_{gNN}$  by setting  $f = \infty$  and  $f' = 1$ . For  $f = \infty$ , the ordered left and bottom lists outside D indicate how  $S_{gNN}$  is updated by adding one-to-one ( $f' = 1$ ) and many-to-many ( $f' = 2$ ) matches. That is, if the same value  $v$  is in the  $i$ -th row of the left list and in the  $j$ -th column of the bottom list, then the match  $(i, j)$  is included into  $S_{gNN}$  as the  $v$ -th element. (b) Given the above keypoint patch configuration, if  $D_{ij} \leq D_{ia} \leq D_{ib} \leq D_{ic}$  in term of descriptor distance, then  $D_{ia}$  is used as denominator for NNR,  $D_{ib}$  for FGNN with center distance, and  $D_{ic}$  for FGNN with overlap error (see text for details, best viewed in color).

case, when the greedy NN is employed with NNR, one have to replace Eq. 2 with an alternative definition

$$D'_{ij} = \frac{D_{ij}}{D_{ij^2 \geq}} \quad (6)$$

$D_{ij^w \geq}$  and  $D_{i^w j \geq}$  are the lowest  $w$ -th values greater or equal to  $D_{ij}$  on the  $j$ -th column and on the  $i$ -th row, respectively. This further constraint is necessary since  $D_{ij}$  may not be equal to  $D_{ij^1}$  so that  $D'_{ij} > 1$ . In order to improve the matching process, a symmetric NNR is proposed in [6] as the harmonic mean between the two entries obtained by swapping the reference image, corresponding to operate on the matrix transpose  $D^\top$  of D

$$D''_{ij} = \frac{2D'_{ij}(D^\top)'_{ji}}{D'_{ij} + (D^\top)'_{ji}} \quad (7)$$

In the particular case of Eq. 6 the harmonic mean becomes

$$D''_{ij} = \frac{2D_{ij}}{D_{ij^2 \geq} + D_{i^2 j \geq}} \quad (8)$$

The First Geometrically Inconsistent NN (FGINN) [62] is another possible improvement to NNR

$$D'_{ij} = \frac{D_{ij}}{D_{ij^2 \circledcirc}} \quad (9)$$

Here, the second lowest value in the denominator of Eq. 2 is intended among those keypoints whose centers are at least  $t_o = 10$  pixels far from the center of the keypoint  $j$  in the corresponding image, denoted as  $D_{ij^2 \circledcirc}$ . The choice of the second lowest value according to FGINN is shown in Fig. 1b. Although the use of keypoint centers implies working on the keypoint space, this approach mainly deals with the descriptor space and it is discussed here. Finally, in [63], many-to-many matching relations have been shown to improve the recall of the matching process, leading to better samples for RANSAC hypothesis generation.

Aimed at incorporating all the matching strategies discussed so far, the blob matching is now formulated according to the following steps.

- 1) The similarity matrix D is pre-filtered so that only matches appearing among the  $f$  best matches for both input pair images will be considered (see Fig. 1a)

$$F = \{D_{ij} \leq D_{ij^f}\} \cup \{D_{ij} \leq D_{ifj}\} \quad (10)$$

- 2) Surviving matches are then filtered according to the greedy approach, modified to take into account the first  $f'$  best matches instead of only the first one. In detail, after being sorted by increasing values,  $D_{ij} \in F$  is added to the multiset  $G$  if both  $(G \cup D_{ij})_{\downarrow \downarrow}$  and  $(G \cup D_{ij})_{\uparrow \uparrow}$  do not contain elements counted more than  $f'$  times (see again Fig. 1a).
- 3) NNR-like similarity values for the matches in  $G$  are obtained by taking into account a many-to-many scheme but also FGNN. Equation 6 is modified to

$$D'_{ij} = \mathcal{D} \quad (11)$$

where  $\mathcal{D}$  can be further specified as

$$\mathcal{D}_{\geq} = \frac{D_{ij}}{D_{ij^2 \geq \circledcirc}} \quad (12)$$

The symbols  $\geq$  and  $\circledcirc$  are the same as for Eqs. 6 and 12, respectively. The threshold  $t_o$  can also express a relative threshold and not only an absolute pixel distance. In the first case, a filtering based on the overlap error between the elliptical patches is considered instead of the original FGINN criterion based on the keypoint center distances (see Fig. 1b). This allows to rely on non-absolute values. A further specialization for  $\mathcal{D}$  is also considered

$$\mathcal{D}_*^+ = \frac{D_{ij}}{D_{ij} + D_{ij^2 \circledcirc}} \quad (13)$$

The  $*$  symbol is a placeholder for  $\geq$ , and can be possible empty, since  $\geq$  is not strictly required to accommodates values into the range  $[0, 1]$ . This holds because the whole column or row spans can be considered instead of limiting the selection only to the values greater than the current value as it was required for  $D_{ij}^2$  in Eq. 6.

4) Lastly, in order to provide the final similarity score  $\bar{D}_{ij}$  for matches in  $G$  to be used for sorting or thresholding match pairs, a function  $\mathcal{W}$  is applied in order to combine the two possible matching similarity values obtained when considering each image as reference. In detail, using the first image as reference corresponds to employ  $D'_{ij}$ , while using the other image corresponds to  $(D^\top)_{ji}'$  so that

$$\bar{D}_{ij} = \mathcal{W}(D'_{ij}, (D^\top)_{ji}')$$
 (14)

$\mathcal{W}(a, b)$  can be simply the projection on one of the two arguments ( $\mathcal{W}(a, b) = a$  or  $\mathcal{W}(a, b) = b$ ), the harmonic mean of Eq. 7 ( $\mathcal{W}(a, b) = (2ab)/(a + b)$ ), and the minimum ( $\mathcal{W}(a, b) = \min(a, b)$ ) or maximum ( $\mathcal{W}(a, b) = \max(a, b)$ ) values of the two arguments, likewise respectively the intersection and union of matching sets employed in [7].

It comes out in Sec. 5.2 that the best blob matching configuration is  $f = 10$ ,  $f' = 5$ ,  $\mathcal{D}^+$  with  $t_o = 10$  px or  $t_o = 75\%$ , and  $\mathcal{W}(a, b) = (2ab)/(a + b)$ . Notice also that blob matching is quite general: By setting  $f = 1$  only mutual NN matches are considered, moving up  $f'$  from 1 when  $f > 1$  the one-to-one match relation becomes a many-to-many relation, FGNN is turned off when  $t_o = \infty$ , and only the first image is used as reference when  $\mathcal{W}(a, b) = a$ .

## 4 DELAUNAY TRIANGULATION MATCHING

Keypoint space context (i.e. the actual image context) is often used to locally constrain matches. Most of the non-model based approaches relies on the concept image local neighborhood, often assumed to be isotropic in order to be captured by the simple Euclidean distance, used to rank closed keypoints [22], [24]. However, due to the non-homogeneous distribution of keypoints on the image, this is not always true and may lead to non-optimal neighborhood estimations. Delaunay triangulation better adapts to this purpose due to its intrinsic capability of handling non-homogeneous spatial distributions. It is well known that both the neighborhood graph and the minimum spanning tree are subsets of the Delaunay triangulation, which also maximized the minimum angle of each triangle mesh. Moreover, Delaunay triangulation can be used to grow up good matches when an initial set of ground-truth matches is provided, as done in [6] with the purpose of benchmarking descriptors. The use of Delaunay triangulation in DTM is twofold: In a first stage  $DTM_1$ , Delaunay triangulation is combined with the greedy matching strategy employed to define  $S_{gNN}$  in Eq. 5 to iteratively prune matches. In a second stage  $DTM_2$ , it is employed to grow up consistent matches from the previously surviving matches.

When computing the Delaunay triangulation, particular attention must be taken to define boundaries. Boundary

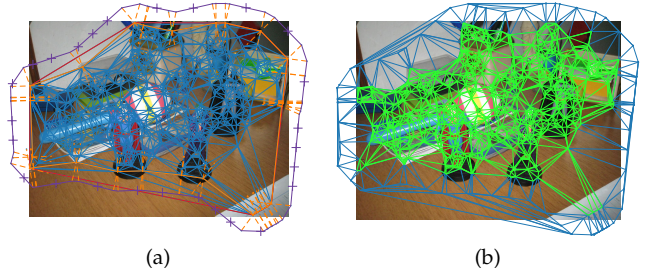


Fig. 2. (left) original Delaunay triangulation using only keypoints (blue), convex hull (red), alpha shape boundary edges (solid orange), border fattenning (dashed orange), and final contour edges (magenta). (right) final Delaunay triangulation with keypoint-only marked edges (green) (see text for details, best viewed in color and zoomed in).

edges of any Delaunay triangulation correspond to the convex hull of the considered keypoints, and triangles for keypoints on the edges of convex hull are generally not well-shaped, i.e. these triangles are far from being almost equilateral. Adding the image corners does not solve the problem as well as breaking the image canvas borders into multiple lines. A more feasible solution would be to expand the boundary edges and split them, where the boundary can be determined by the convex hull or, better, by alpha-shapes<sup>1</sup>, which also relies on Delaunay triangulation. A visual explanation of the different boundary choices is reported in Appendix A, while the alpha shape border computation adopted for DTM is illustrated in Fig. 2. Being  $V$  a keypoint set, alpha-shape boundary edges (solid orange) are extracted and expanded. Specifically, from the two vertexes of each alpha-shape edge, the four points at a fixed distance  $s$  from the edge<sup>2</sup> lying on the line perpendicular to it are included in the set  $B'$  (dashed orange). Alpha-shape boundary edges for  $V \cup B'$  are then extracted and break down into segments of length  $s$ , whose vertexes provide the final boundary point  $B$  for the triangulation (purple).

Given an initial set of matches  $M^0$ , each iteration  $i$  of the  $DTM_1$  stage iteratively prunes  $M^i$  until  $M^i = M^{i-1}$  (see Fig. 3) as described by the following steps:

- 1) Extract keypoint locations for current (surviving) matches. Set  $K_1^i = M^{i-1}$  and  $K_2^i = M^{i-1}$ .
- 2) Construct the current Delaunay triangulation of each image. Round-off keypoint coordinates of  $K_1$  to define the vertex sets  $V_1 = \{([k_x], [k_y]) \in K_1\}$ . From  $V_1$ , compute the boundary set  $B_1^i$  using alpha-shapes as described before, and build the Delaunay triangulation  $\mathcal{T}_1$  for  $I_1$  from  $V_1 \cup B_1^i$  (see Fig. 3, left column). Analogously, define  $V_2$ ,  $B_2^i$  and  $\mathcal{T}_2$  (see Fig. 3, right column). Vertex collapsing by rounding-off avoids many too small triangles that can slow-down the computation.
- 3) Define the local non-isotropic neighborhoods. For each vertex  $v \in V_1$ , define  $A_v^1$  as the set of vertexes adjacent to  $v$  in the triangulation  $\mathcal{T}_1$ , including  $v$  itself. Define also  $M_{A_v^1}^i$  as the set of matches in  $M^{i-1}$  each having the keypoint lying on  $I_1$  collapsed into

1. Using the Matlab `boundary` function with default parameters.
2.  $s$  is empirically set to the minimum between the width and the height of the image divided by 10.

a vertex in  $A_v^1$  by rounding-off, as described before.  $A_v^2$  and  $M_{A_v^2}$  are defined analogously for  $I_2$ .

- 4) *Rank matches according to their spatial coherence.* Assign a rank  $r(m)$  to matches  $m \in M^{i-1}$  collapsed into vertex pair  $(v_l, v_r)$ , by sorting them firstly according to their increasing similarity and then by the decreasing cardinality  $|M_{A_{v_l}^i}^i \cap M_{A_{v_r}^i}^i|$ .
- 5) *Contract the Delaunay triangulations.* Set  $T = \emptyset$ ,  $M' = M^{i-1}$ , and add the match  $m \in M'$  ranked first according to  $r(m)$  to  $T$ . Then remove this match  $m$  from  $M'$  as well as matches in  $(M_{A_{v_l}^i}^i \cup M_{A_{v_r}^i}^i) \setminus (M_{A_{v_l}^i}^i \cap M_{A_{v_r}^i}^i)$ , where  $m$  collapsed into  $(v_l, v_r)$ . Repeat until  $M' = \emptyset$  (see Fig. 3b,d).
- 6) *Expand the Delaunay triangulations.* Define  $M^i$  as the union of the sets  $(M_{A_{v_l}^i}^i \cap M_{A_{v_r}^i}^i)$ , each one obtained from the collapsing pair  $(v_l, v_r)$  a match  $m \in T$  corresponds to (see again Fig. 3b,d).

The set  $M^{\bar{i}}$  at the last iteration  $\bar{i}$  contains the matches survived to the Delaunay triangulation “pulses” (see Fig. 3e). Note that convergence is always guaranteed since by construction the cardinality of  $M^i$  cannot increase with the iterations  $i$ . In the worst case, never seen in practice, no match would be found, i.e.  $M^{\bar{i}} = \emptyset$ .

In order to pick up good matches accidentally discarded at the DTM<sub>1</sub> stage since surrounded only by wrong matches, stage DTM<sub>2</sub> proceeds in reverse order, starting from iteration  $i = \bar{i} - 1$  downto 0, with  $E^{\bar{i}-1} = M^{\bar{i}} = M^{\bar{i}-1}$  by the definition of  $\bar{i}$  given for DTM<sub>1</sub>:

- 1) *Construct the Delaunay triangulations for the (estimated) good matches.* At step  $i$ , compute the Delaunay triangulations  $\mathcal{T}'_1$  and  $\mathcal{T}'_2$  as before, but from the collapsed vertex set of  $E^i$  plus the boundary sets  $B_1^i$  and  $B_2^i$  computed at the DTM<sub>1</sub> stage.
- 2) *Add coherent matches according to the Delaunay triangulations.* Initially set  $E^{i-1} = E^i$ . For each match  $m$  in  $M_i \setminus M^{i-1}$ , find the triangle  $W_1$  of  $\mathcal{T}'_1$  where the corresponding keypoint on  $I_1$  of  $m$  falls into. If the other keypoint on  $I_2$  of  $m$  falls into any triangle on  $I_2$  formed by the corresponding vertexes of  $W_1$ , and this also holds by swapping the role of the images, add the match to  $E^{i-1}$ .

The final set  $E = E^0$  contains the enhanced matches (see Fig. 3f). Notice that stage DTM<sub>2</sub> uses the boundary sets  $B_1$  and  $B_2$  computed in the previous stage DTM<sub>1</sub> in order to increase the chance to include previously discarded keypoints close to the boundary.

## 5 EVALUATION

### 5.1 Setup

The evaluation pipeline is composed by the following steps: keypoint extraction, local descriptor computation, descriptor matching, local spatial filtering and model fitting. For the keypoint extraction the SIFT and HarrisZ detectors are considered, while RootSIFT, RootsGLOH2, HardNet2 and SOSNet are employed as local descriptors. SIFT and RootSIFT are included as standard baselines. Patch orientation is estimated according to [61] for all descriptors,

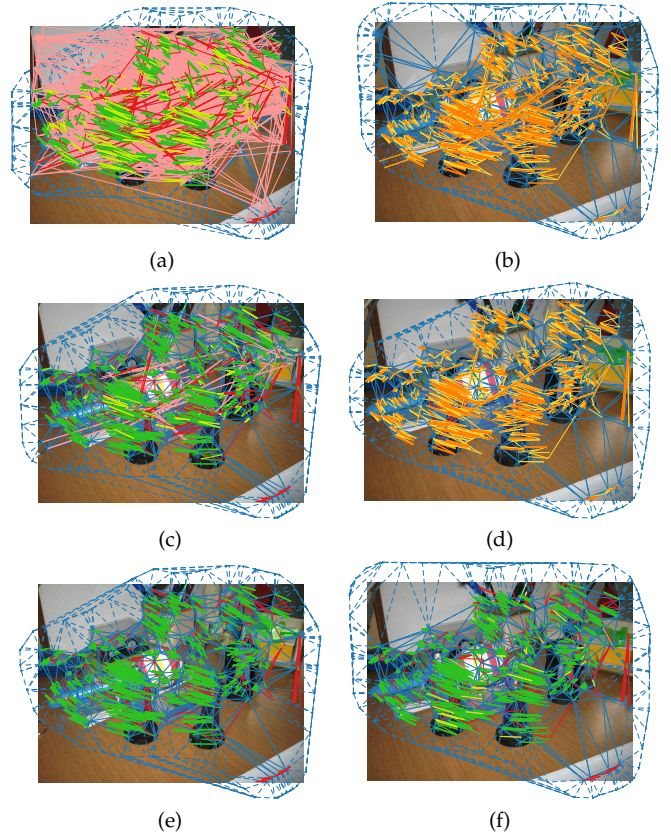


Fig. 3. DTM computation steps. The first and second images of the input pair are superimposed on the left and on the right, respectively, together with their associated Delaunay triangulations (blue). Initial matches are obtained from the best configuration given by HarrisZ+SOSNet with blob matching (see Sec. 5). The first and second iterations  $i$  of the DTM<sub>1</sub> stage are reported as the first and second rows, respectively. For these rows, on the left, clusters of vector flows for retained (green and red) and pruned (yellow and light red) matches are shown. Clusters of correct (green and yellow) and wrong (red and light red) matches can be established as well, according to the evaluation protocol described in Sec. 5. Corresponding contraction (orange) and expansion (yellow) phase clusters are indicated on the right. Image (e) reports the final filtered matches at the sixth last iteration  $\bar{i}$  of DTM<sub>1</sub>, while image (f) shows the final result after the last iteration  $i = 0$  of DTM<sub>2</sub>, colored clusters indicate added (yellow), correct (green and yellow) and wrong (red) matches (see text for details, best viewed in color and zoomed in).

except for RootsGLOH2 that needs no orientation adjusted patches. Descriptor matching, the next step of the pipeline, is achieved only by blob matching, since it behaves as the common descriptor matching strategies with a proper tuning of its parameters. The goal of this evaluation step is to check the advantages offered by match pre-filtering, many-to-many matches, alternative distance definitions and combinations (referring in order to the four different steps of blob matching in Sec. 3). The next step of the pipeline evaluates spatial matching filters, including the proposed DTM and the state-of-the-art, learned or not: LMR, LPM, GLPM, GMS, VFC and LLT. For reference, the standard 0.8 NNR threshold is also included, although not properly a local spatial filter, and indicated as ‘th’, as well as the recent deep model-based OANet. For the last step of the pipeline, being  $q$  the minimal number of matches required to estimate the model<sup>3</sup>, only a simple model estimation using uniquely

3.  $q$  is respectively 4, 8 for homography, fundamental matrix.

one sample made up of the  $3 \times q$  top-ranked surviving matches at the previous step is employed. Although this approach, named 1SAC (one SAmples Consensus) is quite simple, it can give insights about more complex RANSAC approaches. Notice that except for the GLPM, DTM (step 4 of stage DTM<sub>1</sub> in Sec. 4) and OANet other pruning methods do not take into account the descriptor context.

For the evaluation both planar and non-planar scenes are considered, the latter being more complex due to the inclusion of spatial discontinuities caused by occlusion and parallax. In the case of planar scenes, the 15 sequences employed in [6] were used. Each sequence is made up of 6 images where the first one is fixed as reference, for a total of  $19 \times (6 - 1) = 75$  image pairs. In the case of non-planar scenes, besides the 72 image pairs from [6], 27 image pairs already known in the computer vision community were included, for a total of  $72 + 27 = 99$  image pairs. Appendix B shows the scene contained in both datasets.

The proposed evaluation relies on the computation of ground-truth matches. On planar scenes ground-truth correspondences can be easily obtained by estimating the homography that maps one-to-one points across the two scenes [20], [71]. Unlike the planar case, for the non-planar case only a point-to-line mapping through the fundamental matrix is available according to the epipolar geometry. A common approach to evaluate RANSAC-like methods defines inlier matches (hence ground-truth matches) according to the distance between a point and the epipolar line imaging the corresponding point to be matched in the other image (denoted here as method A). However, this approach can lead to many false positive ground-truth matches due to the ambiguity of the map. Other approaches measure the error on the fundamental matrix obtained at the end of matching process with respect to a ground-truth one, which can be estimated by hand-taken correspondences [72] or on the basis of robust SfM approaches [7]. Error distance between corresponding ground-truth and estimated epipolar lines can be considered to judge the goodness of the matching, statistically [73], or on the basis of an homogeneous image sampling [72]. The former approach has been employed in a recent evaluation [44]. Alternatively, the pose error of the camera [7] is obtained from the estimated fundamental matrix (to be understood in a broad sense). Nevertheless, all these evaluations give an indirect measure on the goodness of matches that does not guarantee a true evaluation of the matching process. This happens since there is no direct and clear formula relating fundamental matrix correctness and correct matches, so that from the perspective of evaluating the accuracy of the correspondences, this kind of solutions can be associated to method A. Finally, a further possibility is to compute ground-truth matches by relying on additional constraints induced for instance by employing more images [74] or by manually limiting the spatial localization of the matches [6]. This last solution is adopted in following evaluation according to the protocol described in [6] based on the approximated overlap error (denoted as method B), extended to cope with the issues discussed hereafter. SIFT keypoints included in the evaluation pipeline provide a broader scale range with respect to the HarrisZ keypoints employed in [6]. This implies larger circular patches, with small relative distance between keypoint centers even if the

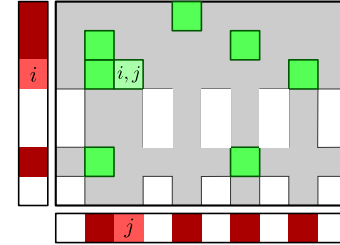


Fig. 4. Visual representation of the normalized recall of a given set of many-to-many matches  $(i, j)$  (green).  $|Z_{\downarrow\downarrow}| = 4$  and  $|Z_{\downarrow\downarrow}| = 5$  by counting the numbers of elements (red) in the row and column outer sets, respectively. In the example  $|Z| = \min(4, 5) = 4$  (see text for details, best viewed in color and zoomed in).

absolute distance measured in pixels is not acceptable by visual inspection. To cope with this, homography reprojection and the epipolar line distance errors are employed (limited to 30 pixels) as additional constraints to the true or approximated overlap errors (limited to 50%), providing visually adequate results (method C). Moreover, taking into account that almost all local spatial filters do not handle the shape and size of the patch, an evaluation based only on the keypoint center distance disregarding the patch overlap can also be conceived to define ground-truth matches (method D). Specifically, in the planar case the distance between a keypoint and the reprojection of the corresponding keypoint in the other image must not exceed 15 pixels. For the non-planar case the epipolar distance must not exceed 15 pixels but the matches must also pass the check defined on the basis of their spatial localizations [6]. With respect to method D, method C obtains a lower number of correct matches due to the scale-based constraints according to the patch shapes. A comparison of the ground-truth estimation methods A, B, C and D is reported in Appendix C, upon which after visual inspection method D has been selected.

Lastly, the definition of recall is adjusted to handle many-to-many matches avoiding apparent boosted results. In particular, using the same notation of Sec. 3, given the set  $Z$  of good matches according to the ground-truth, the associated number of correct matches necessary to compute the recall is defined as  $\min(|Z_{\downarrow\downarrow}|, |Z_{\downarrow\downarrow}|)$  instead of  $|Z|$ , so that multiple keypoint associations are only taken into account once (see Fig. 4). Precision is instead computed as usual. Notice that only in the case of mutual one-to-one matches  $|Z| = \min(|Z_{\downarrow\downarrow}|, |Z_{\downarrow\downarrow}|)$ , so that the new recall definition extends the standard one. This sort of normalization is also employed to compose the top-ranked sample in 1SAC to handle many-to-many matches.

Evaluation code and data are freely available to support the reproducibility of the results<sup>4</sup>.

## 5.2 Blob matching results

Figure 5 shows the heat map depicting the mean Average Precision (mAP) of blob matching for different setups. mAP values are averaged on the whole dataset considering altogether both planar and non-planar scenes, with ground-truth estimated according to method D. For method C,

4. <https://sites.google.com/view/fbellavia/research>  
full benchmark code will be released upon acceptance.

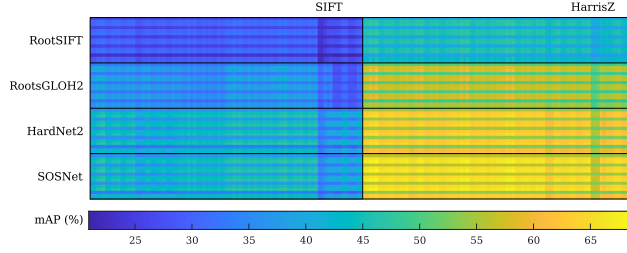


Fig. 5. mAP of blob matching for different setups averaged on the whole image dataset with ground-truth matches estimated by method D (see text for details, best viewed in color).

based on the original patch overlap, similar ranking has been obtained with lower mAP values (not reported). Each rectangular area in Fig. 5 corresponds to a different detector+descriptor pair. Inside each rectangle, a row corresponds to a different combination  $f \times f'$  with  $f \in \{1, 3, 5, 10, \infty\}$  and  $f' \in \{1, 3, 5\}$ . Likewise, each column represents the remaining parameter combinations  $t_o \times \mathcal{D} \times \mathcal{W}$  with  $t_o \in \{\infty, 50\%, 75\%, 99\%, 5 \text{ px}, 10 \text{ px}\}$ ,  $\mathcal{D} = \{\mathcal{D}_{\geq}, \mathcal{D}_{\geq}^+, \mathcal{D}^+\}$  and  $\mathcal{W}(a, b) \in \{a, b, \min(a, b), \max(a, b), (2ab)/(a+b)\}$ . According to Fig. 5, HarrisZ provides better mAP results than SIFT, probably due to the more strict keypoint selection criteria of HarrisZ with respect to SIFT, also leading to a lower number of keypoints for HarrisZ with respect to SIFT. Nevertheless, the number of ground-truth matches is quite similar (928/686, 997/696 matches in the case of planar/non-planar scenes for HarrisZ and SIFT, respectively). Moreover, confirming previous benchmarks SOSNet and HardNet provide the best accuracy results followed by RootsGLOH2 and RootSIFT.

Under the same blob matching setup, mAP correlation between different detector+descriptor pairs is high (more than 90%, except for SIFT+RootsGLOH2 with respect to other detector+descriptor pairs, yet higher than 60%), so that only the best pair HarrisZ+SOSNet is chosen for a more detailed analysis. Figure 6 plots the mAP values for the HarrisZ+SOSNet pair. The  $f \times f'$  pairs  $(\infty, 5)$  and  $(10, 5)$  are those providing the best mAP values (respectively 69% and 68.9%, marked in Fig. 6), while corresponding one-to-one matching setup  $(\infty, 1)$  and  $(10, 1)$  both obtain mAP values less than 57%. This suggests that one-to-one matching can discard a lot of correct candidate matches. Moreover, the close results obtained by  $f = \infty$  and  $f = 10$  indicate that it is sufficient to inspect only the first 10 top-ranked matches when designing a matching strategy. This observation can be exploited to improve computational efficiency since many wrong matches can be discarded a priori.

Figure 7a plots the mAP values for the remaining blob matching parameters for the best configuration found so far. For reference, the corresponding plot in the case of SIFT+RootSIFT is reported in Fig. 7b. According to the plots, FGNN with  $t_o = 75\%$  or  $t_o = 10 \text{ px}$  provides overall the best results. Results with  $t_o = 50\%$  or  $t_o = 75\%$  in Fig. 7a and Fig. 7b are less consistent and more unstable, maybe due to the own characteristics of the keypoint detectors, providing patches with different shapes (circular for SIFT, elliptical for HarrisZ) and scale ranges.  $\mathcal{D}^+$  provides better results as FGNN range increases. This is reasonably

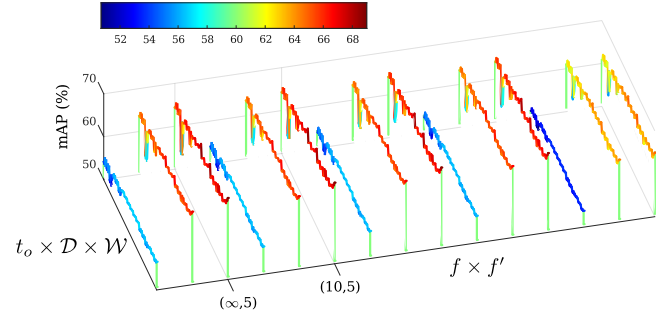


Fig. 6. mAP of blob matching with HarrisZ+SOSNet for different setups averaged on the whole image dataset with ground-truth matches estimated by method D (see text for details, best viewed in color).

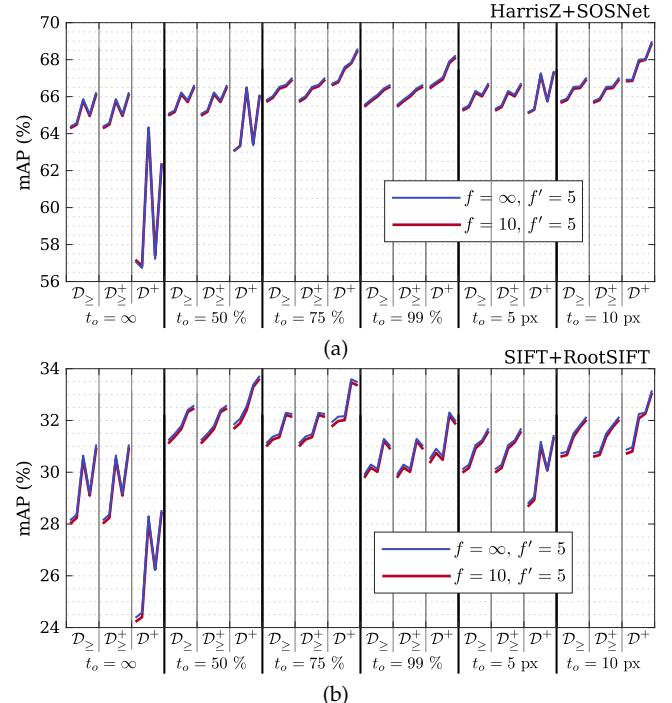


Fig. 7. Detailed mAP results of blob matching with (a) HarrisZ+SOSNet and (b) SIFT+RootSIFT for different setups averaged on the whole dataset.  $\mathcal{W}(a, b)$  values corresponding to  $a, b, \min(a, b), \max(a, b)$  and  $(2ab)/(a+b)$  are reported in order inside each vertical sub-band (see text for details, best viewed in color and zoomed in).

expected due to its design, while  $\mathcal{D}^+$  does not provide any improvement with respect to  $\mathcal{D}_{\geq}$ . Finally, inside each band of the plots, mAP values are reported in order considering the different  $\mathcal{W}$  possibilities. While there is no evident difference using one image or another as reference, their combined distances improve the results. In particular, the minimum seems to achieve better results when FGNN has no or small ranges, on the opposite of the maximum, and in any case the harmonic mean equals or surpasses the best among the previous  $\mathcal{W}$  choices. As observed in [7], the more the matches are discriminative (that happens when FGNN is employed with a sufficient range) the more their combination by union (which equivalent to use the maximum) is better, and the opposite holds for their intersection (which is equivalent to use the minimum). According to this results the best blob matching setup is  $f = 10, f' = 5, \mathcal{D}^+$  with  $t_o = 10 \text{ px}$  or  $t_o = 75\%$ , and  $\mathcal{W}(a, b) = (2ab)/(a+b)$ .

### 5.3 Delaunay Triangulation Matching results

Figure 8 plots the average precision and recall values on planar and non-planar scenes for the evaluated local spatial filters, without or with 1SAC applied as post-processing. Results are reported by considering the global behavior (left column), i.e. averaging the results over all the considered detectors, descriptors and blob matching setups, the baseline configuration as reference (middle column), i.e. SIFT+RootSIFT with the one-to-one NNR greedy matching obtained by setting  $f = \infty$ ,  $f' = 1$ ,  $t_o = \infty$ ,  $\mathcal{D}_{\geq}$ ,  $\mathcal{W} = a$ , and the best configuration so far (right column), i.e. HarrisZ+SOSNet with blob matching setup  $f = 10$ ,  $f' = 5$ ,  $t_o = 0.75$ ,  $\mathcal{D}^+$ ,  $\mathcal{W} = 2ab/(a+b)$ . Detailed statistics including precision, recall, the number of correct and output matches, the number of times a method failed, and the running time are reported in Appendix D. The recall is computed considering only ground-truth matches from the current blob matching setup used in the pipeline with those provided by OANet. OANet matches are included together with blob matches since OANet works on the same level of blob matching, i.e. OANet cannot directly filters a given set of input matches. No precision/recall aggregated measures, such as mAP or  $F_\beta$  score are considered in the evaluation. On one hand, mAP requires that the number of output matches should be approximately the same for all methods since it is very sensitive to the recall, otherwise the highest scores would be assigned to the methods providing more output matches, including the initial blob matching. On the other hand, the choice of the  $\beta$  parameter in  $F_\beta$  can be questionable, as well as the choice of the recall normalization factor (see again Appendix D for further details), promoting one method or another without reflecting their effective performances. Nevertheless, mAP,  $F_1$  and  $F_{0.5}$  scores are reported in the additional material for completeness.

The average planar/non-planar number of ground-truth matches per image pair are 551/429, 367/257, 681/575 for the global, reference and best configurations, respectively. The planar case is more easy than the non-planar case according to the number of correct matches retrieved. By inspecting Fig. 8, all methods improve the precision with respect to the blob matching, that obviously achieve the highest recall. Concerning the precision, in the planar case almost all methods are well aligned, what really changes is the attained recall. For planar scenes, VFC provides concurrently the best precision and recall in any configuration, followed by the full-stage DTM (DTM<sub>2</sub>). The first stage of DTM (DTM<sub>1</sub>) provides a similar precision but lower recall. The simple threshold th obtains high precision but in general low recall, that increases when better matches are provided as input in the best configuration. OANet behaves similarly, with very high precision but low recall, that notably increases in the baseline configuration on which the network as been trained, showing an actual issue of learning-based approaches. This observation also holds for LMR, that in general provides higher recall than OANet. Notice also that OANet precision is higher since it is model-based, while other approaches are not. LPM seems again to work better with the baseline configuration it was designed for, however GLPM, which is an extension of LPM where the initial neighborhoods are obtained by a

stricter thresholding, can provide better results, especially in terms of recall, for the best configuration. These results are comparable with those of DTM<sub>1</sub>, underlining the goodness of the neighborhood relations computed from Delaunay triangulations. GMS precision and recall are in general lower than those of other competitors, except in the best configuration. In fact, GMS was originally designed to work with a considerable number of matches. LLT obtains the lowest scores. Finally, the simple model-based 1SAC improves the precision but lowers the recall, maintaining the ranking almost unaltered. Note that the blob matching after 1SAC post-filtering achieves almost the same results of VFC, the best local spatial filter in the planar case, apparently making avoidable to use local spatial filters. This is not true because planar images are relatively easy, homographies provide one-to-one point maps between images, and 1SAC re-filters the output of the local spatial filters. These observations imply that homographies are almost correctly estimated by all methods, and in this case higher recall is obtained as more input matches are provided.

The non-planar case is more difficult. Unlike the planar case, VFC seems to suffer the major complexity of non-planar scenes, attaining a precision among the worst values, while DTM is still well balanced. Full-stage DTM and DTM<sub>1</sub> have quite similar precision values, but the former provides again higher recall. Most of the previous observations done for each spatial filtering method in the planar case are still valid. However, simple thresholding and GLPM, seem unable to get the same recall ranks observed for the planar case, maybe due to the lesser effectiveness of the thresholding criterion. Notice that unlikely the planar case, blob matching with 1SAC is unable to achieve a level of precision comparable to the one achieved by local spatial filters, yet providing a gain in terms of recall. Nevertheless, recall is less critical for the whole pipeline performances.

The number of times the local spatial filters failed to get at least one correct matches (reported on Appendix D) can provide clues about each method robustness. For both planar or non-planar scenes, excluding obviously the blob matching, DTM obtained the highest rank, followed by LMR, and the simple threshold th. LPM follows with VFC, then GLPM. GMS and LLT close the ranking. Under these observations, although on planar scenes VFC can be said to achieve the best results in terms of precision and recall, while DTM comes next, in terms of method stability and robustness DTM may be preferable. Notice that when 1SAC post-filtering is applied more failures arise, as the number of putative matches is reduced.

Visual qualitative analysis according to the examples reported in Appendix D agrees with the quantitative results discussed above. VFC is very effective in the presence of large planar structures but in the other cases it may leave in many outliers. OANet is quite accurate but can leave out many inliers, especially in the presence repeated patterns. GMS does not work well when consistent clusters of outliers are predominant. Simple threshold th is in general adequate, but can leave out many inliers, decreasing successive model estimation accuracy. LPM, LMR and DTM increasingly include more inliers and thus improve the recall, maintaining a low number of outliers. DTM results are the most balanced overall, thanks to the neighborhood definition in terms of

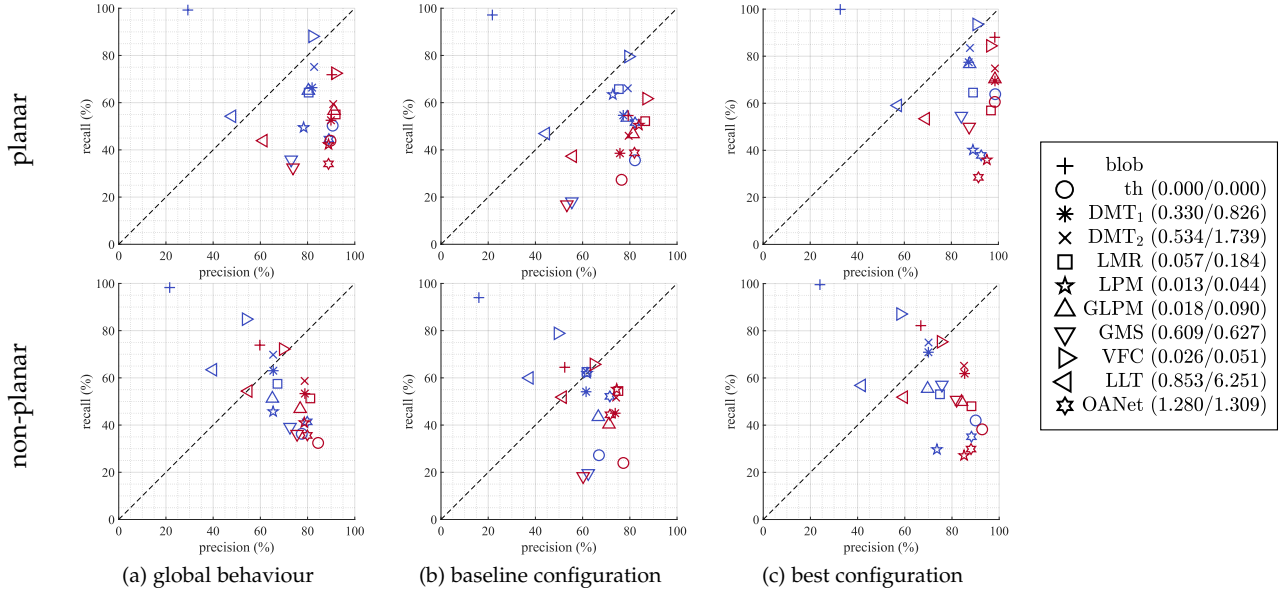


Fig. 8. Average precision/recall values of the local spatial filters for planar and non planar scenes. The recall is computed with respect to the union of ground truth matches in blob matching and OANet ( $\text{blob} \cup \text{OANet}$ ), results without/with 1SAC are in blue/red. Average running times (s) for the baseline/best configurations are reported alongside in the legend. (a) Results averaged over all tested keypoint detectors, descriptors and blob matching setups, the average planar/non-planar number of ground-truth matches per image pair are 551/429 ( $\text{blob} \cup \text{OANet}$ ), 963/691 (all matches), (b) baseline reference configuration, average planar/non-planar number of ground-truth matches per image pair are 367/257 ( $\text{blob} \cup \text{OANet}$ ), 997/696 (all matches), (c) best configuration, the average planar/non-planar number of ground-truth matches per image pair are 681/575 ( $\text{blob} \cup \text{OANet}$ ), 928/686 (all matches) (see text for details, best viewed in color and zoomed in).

Delaunay triangulation in conjunction with the injection of some descriptor space context knowledge, unlike LMR and LPM that only rely on the position of keypoints. GLPM results dangle between those of LPM and th, while LLT has in general a high number of outliers.

Average running times (s) are reported in Fig. 8 alongside the legend for the baseline/best configurations that imply one-to-one and many-to-many matching relations, respectively. Results have been obtained with a Ubuntu 19.10 system running on an Intel Core i5 with 32 GB of RAM and without GPU acceleration. The original code was used for each implementation. OANet and GMS are implemented in Python, the remaining methods in Matlab and, with the exception of DTM, contain mex C code to speed-up the computation. The running times increase proportionally to the number of input matches by at least a linear factor, from the baseline configuration using one-to-one matches to the best configuration using many-to-many matches. This factor is theoretically expected to be around  $\sum_{i=1}^{f'} \frac{i}{f'} = 3$  since  $f' = 5'$  for the best setup. According to the running times reported in Fig. 8, simple threshold th is clearly the fastest approach, followed by LPM, GLPM, VFC and LMR. GMS and DTM<sub>1</sub> follow, then the full-stage DTM and OANet, and finally LLT with the highest running time. Notice that better running times are expected for OANet on GPU and, likewise, better running times are also expected for DTM with optimized code. The various steps of DTM can be highly parallelized and, in the same manner of LPM, portions of its code would benefit of mex C code rewriting<sup>5</sup>.

5. According to the author's experience Matlab is not the best environment for graph manipulations.

## 6 CONCLUSIONS AND FUTURE WORK

This paper analyzes the local image descriptor matching problem according to two possible contexts that can be used to characterize images, and to improve the number of correct correspondences.

The first context is provided by the descriptor space. The novel general blob matching strategy is designed to incorporate different approaches for a clear and detailed analysis of the aspects that characterize the basic matching strategies. According to the evaluation, pre-filtering, many-to-many matches, two-way comparisons using symmetric distances and a good choice of the second best match in NNR can improve the matching process.

The second context is provided by the keypoint space, i.e. the actual image space. A new local spatial filter named DTM is proposed. DTM extracts spatial neighborhood relations between keypoints by Delaunay triangulation, alternating triangulation contractions and expansions to remove inconsistent matches and to include putative matches. DTM is very robust and obtains comparable or better results with respect to the state-of-the-art, especially in the more complex non-planar scenario.

Although blob matching and DTM mainly operate respectively on the descriptor and space contexts, they both betray contaminations from the other context, underlining the need of fully integrating different contexts to go beyond the current state-of-the-art.

Finally a comprehensive evaluation of the main phases of the matching pipeline is carried out, based on a new benchmark, focusing on the estimation of correct matches and not on their effects on the scene. The analysis considers both blob and corner like keypoints, among the best local image descriptors so far, several image matching strate-

gies, state-of-the-art local spatial filters, and also the simple model-based filter. It clearly emerges from the results that combining the different method can offer a clear advantage with respect to the baseline SIFT matching strategy.

As future work, further possibilities for merging matching strategies will be investigated, as well as mesh-based applications of the triangulation in order to grow up matches and to obtain semi-dense correspondences. Additionally, it would be interesting to analyze how triangulations could be used for clustering and for spatially characterizing the objects in the scene. Further research directions will be also aimed at improving the benchmark, by extending the datasets with more image pairs and by designing better error metrics to compare the different approaches.

## ACKNOWLEDGMENT

The Titan Xp used for this research was generously donated by the NVIDIA Corporation.

F. Bellavia is currently funded by the Italian Ministry of Education and Research (MIUR) under the program PON Ricerca e Innovazione 2014-2020, cofunded by the European Social Fund (ESF), CUP B74I18000220006, id. proposta AIM 1875400, linea di attività 2, Area Cultural Heritage.

## REFERENCES

- [1] N. Snavely, S. Seitz, and R. Szeliski, "Modeling the world from internet photo collections," *International Journal of Computer Vision*, vol. 80, no. 2, pp. 189–210, 2008.
- [2] M. Brown and D. G. Lowe, "Automatic panoramic image stitching using invariant features," *International Journal of Computer Vision*, vol. 74, no. 1, pp. 59–73, Aug 2007.
- [3] L. Zheng, Y. Yang, and Q. Tian, "SIFT meets CNN: A decade survey of instance retrieval," *IEEE Transactions on Pattern Analysis and Machine Intelligence*, vol. 40, no. 5, pp. 1224–1244, 2018.
- [4] R. Mur-Artal, J. Montiel, and J. Tardos, "ORB-SLAM: a versatile and accurate monocular slam system," *IEEE Transactions on Robotics*, vol. 31, no. 5, pp. 1147–1163, 2015.
- [5] D. Lowe, "Distinctive image features from scale-invariant keypoints," *International Journal of Computer Vision*, vol. 60, no. 2, pp. 91–110, 2004.
- [6] F. Bellavia and C. Colombo, "Is there anything new to say about SIFT matching?" *International Journal of Computer Vision*, 2020.
- [7] Y. Jin, D. Mishkin, A. Mishchuk, J. Matas, P. Fua, K. M. Yi, and E. Trulls, "Image matching across wide baselines: From paper to practice," in *arXiv*, 2020.
- [8] R. Arandjelović and A. Zisserman, "Three things everyone should know to improve object retrieval," in *Proceedings of the IEEE Conference on Computer Vision and Pattern Recognition (CVPR)*, 2012, pp. 2911–2918.
- [9] Y. Ke and R. Sukthankar, "PCA-SIFT: a more distinctive representation for local image descriptors," in *Proceedings of the IEEE Conference on Computer Vision and Pattern Recognition (CVPR)*, vol. 2, 2004, pp. 506–513.
- [10] J. Dong and S. Soatto, "Domain-size pooling in local descriptors: DSP-SIFT," in *Proceedings of the IEEE Conference on Computer Vision and Pattern Recognition (CVPR)*, 2015.
- [11] F. Bellavia and C. Colombo, "Rethinking the sGLOH descriptor," *IEEE Transactions on Pattern Analysis and Machine Intelligence*, vol. 40, no. 4, pp. 931–944, 2018.
- [12] —, "Which is Which? Evaluation of local descriptors for image matching in real-world scenarios," in *International Conference on Computer Analysis of Images and Patterns (CAIP)*, 2019. [Online]. Available: <http://cvg.dsi.unifi.it/wisw.caip2019>
- [13] J. L. Schönberger and J. M. Frahm, "Structure-from-Motion revisited," in *Conference on Computer Vision and Pattern Recognition (CVPR)*, 2016.
- [14] Z. Luo, T. Shen, L. Zhou, J. Zhang, Y. Yao, S. Li, T. Fang, and L. Quan, "ContextDesc: Local descriptor augmentation with cross-modality context," *Computer Vision and Pattern Recognition (CVPR)*, 2019.
- [15] V. Balntas, E. Riba, D. Ponsa, and K. Mikolajczyk, "Learning local feature descriptors with triplets and shallow convolutional neural networks," in *Proceedings of the British Machine Vision Conference (BMVC)*, 2016, pp. 119.1–119.11.
- [16] Y. Tian, B. Fan, and F. Wu, "L2-Net: deep learning of discriminative patch descriptor in euclidean space," in *IEEE Conference on Computer Vision and Pattern Recognition (CVPR)*, 2017, pp. 6128–6136.
- [17] A. Mishchuk, D. Mishkin, F. Radenovic, and J. Matas, "Working hard to know your neighbor's margins: Local descriptor learning loss," in *Advances in Neural Information Processing Systems 30: Annual Conference on Neural Information Processing Systems (NIPS)*, 2017, pp. 4829–4840.
- [18] Z. Luo, T. Shen, L. Zhou, S. Zhu, R. Zhang, Y. Yao, T. Fang, and L. Quan, "Geodesc: Learning local descriptors by integrating geometry constraints," in *Proceedings of the European Conference on Computer Vision (ECCV)*, 2018.
- [19] Y. Tian, X. Yu, B. Fan, F. Wu, H. Heijnen, and V. Balntas, "SOSNet: Second order similarity regularization for local descriptor learning," in *CVPR*, 2019.
- [20] V. Balntas, K. Lenc, A. Vedaldi, and K. Mikolajczyk, "HPatches: A benchmark and evaluation of handcrafted and learned local descriptors," in *IEEE Conference on Computer Vision and Pattern Recognition (CVPR)*, 2017, pp. 3852–3861.
- [21] Z. Li and N. Snavely, "MegaDepth: Learning single-view depth prediction from internet photos," in *Computer Vision and Pattern Recognition (CVPR)*, 2018.
- [22] J. Ma, J. Zhao, J. Jiang, H. Zhou, and X. Guo, "Locality preserving matching," *International Journal of Computer Vision*, vol. 127, no. 5, pp. 512–531, May 2019.
- [23] J. W. Bian, W. Y. Lin, Y. Liu, L. Zhang, S. K. Yeung, M. M. Cheng, and I. Reid, "GMS: Grid-based motion statistics for fast, ultra-robust feature correspondence," *International Journal of Computer Vision*, 2019.
- [24] J. Ma, X. Jiang, J. Jiang, J. Zhao, and X. Guo, "LMR: Learning a two-class classifier for mismatch removal," *IEEE Transactions on Image Processing*, vol. 28, no. 8, pp. 4045–4059, 2019.
- [25] J. Ma, J. Jiang, H. Zhou, J. Zhao, and X. Guo, "Guided locality preserving feature matching for remote sensing image registration," *IEEE Transactions on Geoscience and Remote Sensing*, vol. 56, no. 8, pp. 4435–4447, 2018.
- [26] J. Ma, J. Zhao, J. Tian, A. L. Yuille, and Z. Tu, "Robust point matching via vector field consensus," *IEEE Transactions on Image Processing*, vol. 23, no. 4, pp. 1706–1721, 2014.
- [27] J. Ma, H. Zhou, J. Zhao, Y. Gao, J. Jiang, and J. Tian, "Robust feature matching for remote sensing image registration via locally linear transforming," *IEEE Transactions on Geoscience and Remote Sensing*, vol. 53, no. 12, pp. 6469–6481, 2015.
- [28] W. Lin, F. Wang, M. Cheng, S. Yeung, P. H. S. Torr, M. N. Do, and J. Lu, "Code: Coherence based decision boundaries for feature correspondence," *IEEE Transactions on Pattern Analysis and Machine Intelligence*, vol. 40, no. 1, pp. 34–47, 2018.
- [29] X. Jiang, J. Ma, J. Jiang, and X. Guo, "Robust feature matching using spatial clustering with heavy outliers," *IEEE Transactions on Image Processing*, vol. 29, pp. 736–746, 2020.
- [30] C. Zhao, Z. Cao, J. Yang, K. Xian, and X. Li, "Image feature correspondence selection: A comparative study and a new contribution," *IEEE Transactions on Image Processing*, vol. 29, pp. 3506–3519, 2020.
- [31] R. I. Hartley and A. Zisserman, *Multiple View Geometry in Computer Vision*. Cambridge University Press, 2000.
- [32] M. Fischler and R. Bolles, "Random sample consensus: A paradigm for model fitting with applications to image analysis and automated cartography," *Communications of the ACM*, vol. 24, no. 6, pp. 381–395, 1981.
- [33] O. Chum and J. Matas, "Matching with PROSAC - progressive sample consensus," in *Proceedings of the IEEE Conference on Computer Vision and Pattern Recognition (CVPR)*, 2005, pp. 220–226.
- [34] T. Sattler, B. Leibe, and L. Kobbelt, "SCRAMSAC: Improving RANSAC's efficiency with a spatial consistency filter," in *Proceedings of the IEEE International Conference on Computer Vision (ICPR)*, 2009, pp. 2090–2097.
- [35] R. Raguram, O. Chum, M. Pollefeys, J. Matas, and J. Frahm, "USAC: A universal framework for random sample consensus," *IEEE Transactions on Pattern Analysis and Machine Intelligence*, vol. 35, no. 8, pp. 2022–2038, 2013.

[36] D. Barath and J. Matas, "Graph-Cut RANSAC," in *Proceedings of the IEEE Conference on Computer Vision and Pattern Recognition (CVPR)*, 2018, pp. 6733–6741.

[37] E. Brachmann and C. Rother, "Neural-guided RANSAC: Learning where to sample model hypotheses," in *Proceedings of the IEEE International Conference on Computer Vision (ICCV)*, 2019.

[38] K. M. Yi, E. Trulls, V. Lepetit, and P. Fua, "Lift: Learned invariant feature transform," in *Proceedings of the European Conference on Computer Vision (ECCV)*, 2016.

[39] Y. Ono, E. Trulls, P. Fua, and K. M. Yi, "LF-Net: Learning local features from images," in *Proceedings of the 32nd Conference on Neural Information Processing Systems (NeurIPS) 2018*, 2018.

[40] D. DeTone, T. Malisiewicz, and A. Rabinovich, "Superpoint: Self-supervised interest point detection and description," in *The IEEE Conference on Computer Vision and Pattern Recognition (CVPR) Workshops*, June 2018.

[41] H. Noh, A. Araujo, J. Sim, T. Weyand, and B. Han, "Large-scale image retrieval with attentive deep local features," in *The IEEE International Conference on Computer Vision (ICCV)*, Oct 2017.

[42] M. Dusmanu, I. Rocco, T. Pajdla, M. Pollefeys, J. Sivic, A. Torii, and T. Sattler, "D2-Net: A Trainable CNN for Joint Detection and Description of Local Features," in *Proceedings of the 2019 IEEE Conference on Computer Vision and Pattern Recognition (CVPR)*, 2019.

[43] P. E. Sarlin, D. DeTone, T. Malisiewicz, and A. Rabinovich, "SuperGlue: Learning feature matching with graph neural networks," in *arXiv*, 2019.

[44] J. W. Bian, Y. H. Wu, J. Zhao, Y. Liu, L. Zhang, M. M. Cheng, and I. Reid, "An evaluation of feature matchers for fundamental matrix estimation," in *Proceedings of the British Machine Vision Conference (BMVC)*, 2019.

[45] C. Harris and M. Stephens, "A combined corner and edge detector," in *Proceedings of the 4th Alvey Vision Conference*, 1988, pp. 147–151.

[46] K. Mikolajczyk and C. Schmid, "Scale & affine invariant interest point detectors," *International Journal of Computer Vision*, vol. 60, no. 1, pp. 63–86, 2004.

[47] H. Bay, A. Ess, T. Tuytelaars, and L. Van Gool, "Speeded-up robust features (SURF)," *Computer Vision and Image Understanding*, vol. 110, no. 3, pp. 346–359, 2008.

[48] S. Leutenegger, M. Chli, and R. Siegwart, "BRISK: Binary robust invariant scalable keypoints," in *Proceedings of the IEEE International Conference on Computer Vision (ICCV)*, 2011.

[49] E. Rublee, V. Rabaud, K. Konolige, and G. Bradski, "ORB: an efficient alternative to SIFT or SURF," in *Proceedings of the IEEE International Conference on Computer Vision (ICCV)*, 2011, pp. 2564–2571.

[50] A. Barroso-Laguna, E. Riba, D. Ponsa, and K. Mikolajczyk, "KeyNet: Keypoint detection by handcrafted and learned CNN filters," in *Proceedings of the International Conference on Computer Vision (ICCV)*, 2019.

[51] F. Bellavia, D. Tegolo, and C. Valenti, "Improving Harris corner selection strategy," *IET Computer Vision*, vol. 5, no. 2, pp. 86–96, 2011.

[52] P. F. Alcantarilla, J. Nuevo, and A. Bartoli, "Fast explicit diffusion for accelerated features in nonlinear scale space," in *Proceedings of the British Machine Vision Conference (BMVC)*, 2013.

[53] B. Fan, F. Wu, and Z. Hu, "Rotationally invariant descriptors using intensity order pooling," *IEEE Transactions on Pattern Analysis and Machine Intelligence*, vol. 34, no. 10, pp. 2031–2045, 2012.

[54] Z. Wang, B. Fan, and F. Wu, "Local intensity order pattern for feature description," in *Proceedings of the IEEE International Conference on Computer Vision (ICCV)*, 2011, pp. 603–610.

[55] E. Tola, V. Lepetit, and P. Fua, "Daisy: an efficient dense descriptor applied to wide baseline stereo," *IEEE Transactions on Pattern Analysis and Machine Intelligence*, vol. 32, no. 5, pp. 815–830, 2010.

[56] C. Strecha, A. Bronstein, M. Bronstein, and P. Fua, "LDAHash: Improved matching with smaller descriptors," *IEEE Transactions on Pattern Analysis and Machine Intelligence*, vol. 34, no. 1, pp. 66–78, 2012.

[57] A. Bursuc, G. Tolias, and H. Jégou, "Kernel Local Descriptors with Implicit Rotation Matching," in *ACM International Conference on Multimedia Retrieval (ICMR)*, 2015.

[58] F. Bellavia and C. Colombo, "RootsGLOH2: embedding RootSIFT "square rooting" in sGLOH2," *IET Computer Vision*, 2020.

[59] M. Pultar, D. Mishkin, and J. Matas, "Leveraging outdoor webcams for local descriptor learning," in *Proceedings of Computer Vision Winter Workshop (CVWW) 2019*, 2019.

[60] D. Mishkin, F. Radenovic, and J. Matas, "Repeatability is not enough: Learning affine regions via discriminability," in *Proceedings of the European Conference on Computer Vision (ECCV)*, 2018.

[61] K. Yi, Y. Verdie, P. Fua, and V. Lepetit, "Learning to assign orientations to feature points," in *Proceedings of the IEEE Conference on Computer Vision and Pattern Recognition (CVPR)*, 2016, pp. 1–8.

[62] K. Lenc, J. Matas, and D. Mishkin, "A few things one should know about feature extraction, description and matching," in *Proceedings of the Computer Vision Winter Workshop (CVWW)*, 2014, pp. 67–74.

[63] W. Zhang and J. Kosecka, "Generalized RANSAC framework for relaxed correspondence problems," in *Proceeding of the International Symposium on 3D Data Processing, Visualization, and Transmission (3DPVT)*, 2006, pp. 854–860.

[64] J. Morel and G. Yu, "ASIFT: A new framework for fully affine invariant image comparison," *SIAM Journal on Imaging Sciences*, vol. 2, no. 2, pp. 438–469, 2009.

[65] V. Ferrari, T. Tuytelaars, and Luc Val Gool, "Wide-baseline multiple-view correspondences," in *Proceedings of the IEEE Conference on Computer Vision and Pattern Recognition (CVPR)*, 2003.

[66] A. Geiger, J. Ziegler, and C. Stiller, "Stereoscan: Dense 3D reconstruction in real-time," in *Proceedings of the IEEE Intelligent Vehicles Symposium (IV)*, 2011.

[67] A. S. Brahmachari and S. Sarkar, "BLOGS: Balanced local and global search for non-degenerate two view epipolar geometry," in *Proceedings of the IEEE International Conference on Computer Vision (ICCV)*, 2009, pp. 1685–1692.

[68] L. Magri and A. Fusiello, "T-linkage: A continuous relaxation of j-linkage for multi-model fitting," in *Proceedings of the IEEE Conference on Computer Vision and Pattern Recognition (CVPR)*, 2014, pp. 3954–3961.

[69] K. M. Yi, E. Trulls, Y. Ono, V. Lepetit, M. Salzmann, and P. Fua, "Learning to find good correspondences," in *Proceedings of the IEEE Conference on Computer Vision and Pattern Recognition (CVPR)*, 2018.

[70] J. Zhang, D. Sun, Z. Luo, A. Yao, L. Zhou, T. Shen, Y. Chen, H. Liao, and L. Quan, "Learning two-view correspondences and geometry using order-aware network," in *Proceedings of the IEEE International Conference on Computer Vision (ICCV)*, 2019, pp. 5844–5853.

[71] K. Mikolajczyk and C. Schmid, "A performance evaluation of local descriptors," *IEEE Transactions on Pattern Analysis and Machine Intelligence*, vol. 27, no. 10, pp. 1615–1630, 2005.

[72] D. Tegolo and F. Bellavia, "noRANSAC for fundamental matrix estimation," in *Proceedings of the British Machine Vision Conference (BMVC)*, 2011.

[73] Z. Zhang, "Determining the epipolar geometry and its uncertainty: A review," *International Journal of Computer Vision*, vol. 27, no. 2, pp. 161–195, 1998.

[74] P. Moreels and P. Perona, "Evaluation of features detectors and descriptors based on 3d objects," *International Journal of Computer Vision*, vol. 73, no. 3, pp. 263–284, 2007.

## APPENDIX A DTM BORDER COMPUTATION

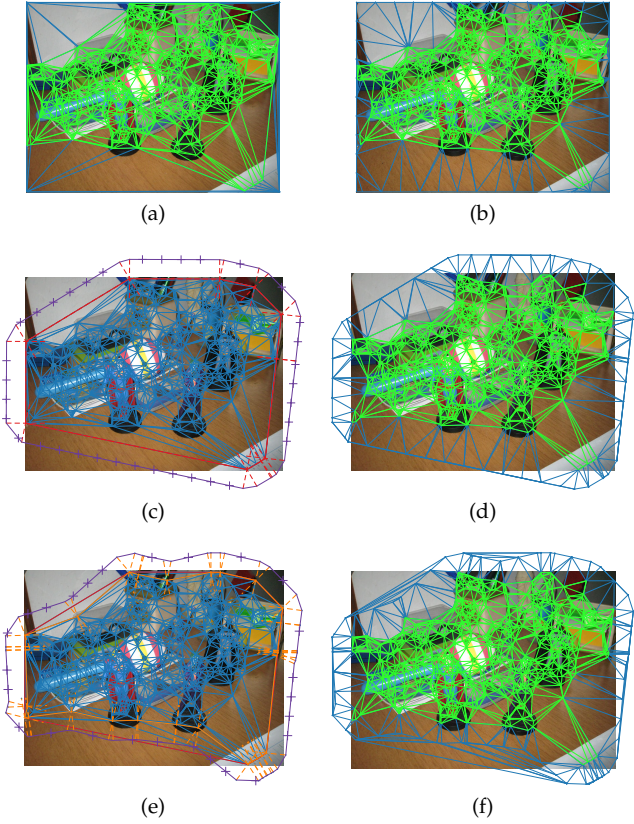


Fig. 9. Delaunay triangulations by including image corners (a) and by breaking the canvas borders into multiple lines (b). (c) Convex hull (solid red) fattening (dashed red) in order to obtain expanded contour edges (purple) with the resulting Delaunay triangulation (d). (e) Analogous results using alpha-shape boundary edges (orange) and (f) the final Delaunay triangulation employed in DTM. Green edges are used to distinguish edge-connecting keypoints from the others (see Sec. 4 for details, best view in color and zoomed in).

## APPENDIX B EVALUATION DATASET

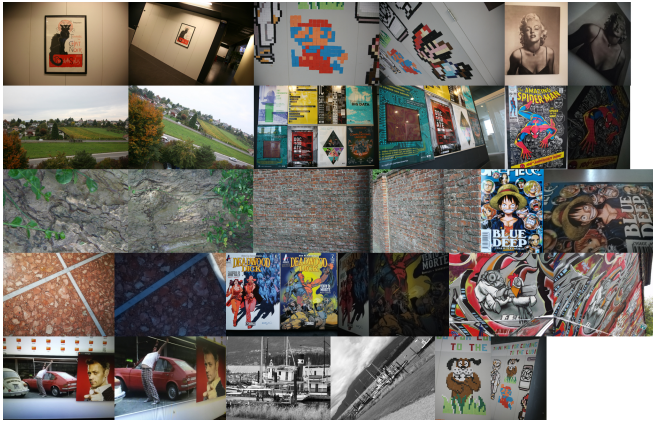


Fig. 10. Image thumbnails of the planar dataset. Each scene is made up of six images, only two of these are shown (see Sec. 5.1 for details, best viewed in color and zoomed in).

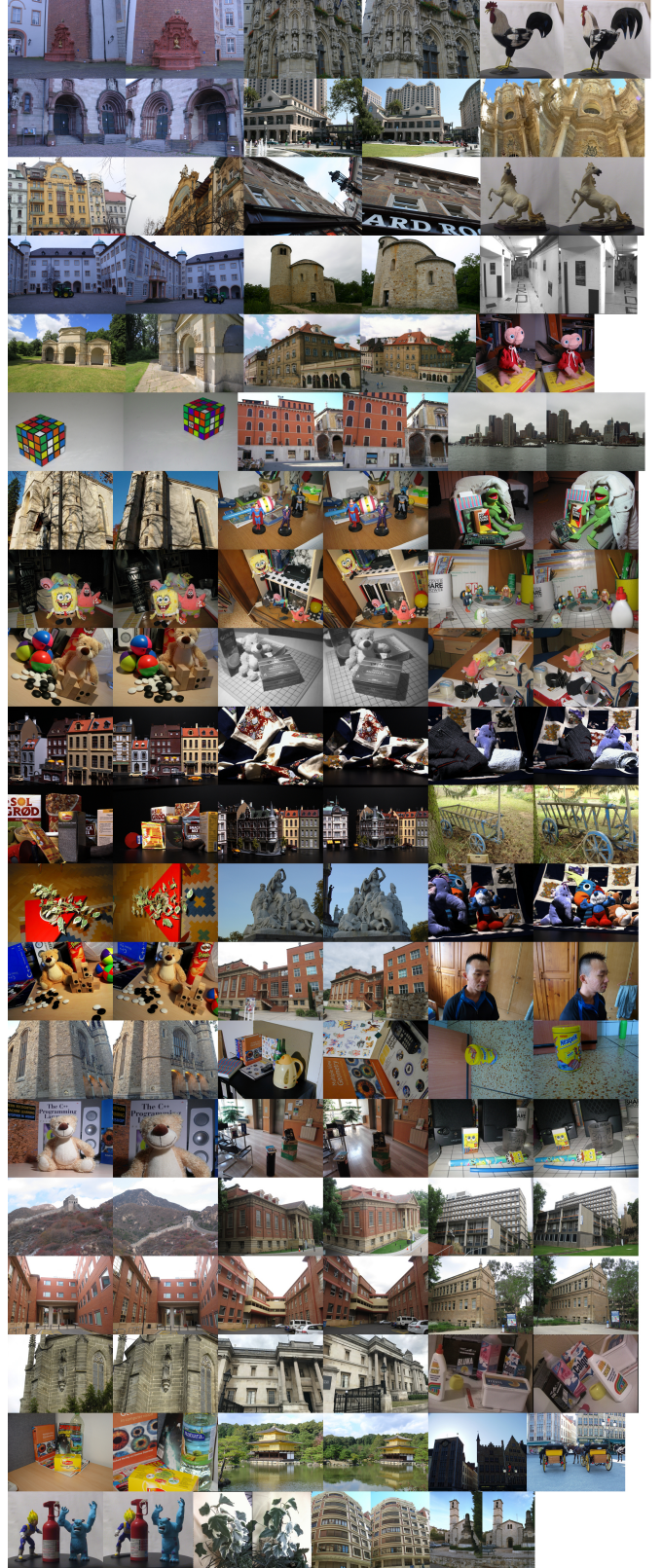


Fig. 11. Image thumbnails of the non-planar dataset. Each scene is made up of two or three images, only two of these are shown (see Sec. 5.1 for details, best viewed in color and zoomed in).

## APPENDIX C

### GROUND TRUTH ESTIMATION METHODS

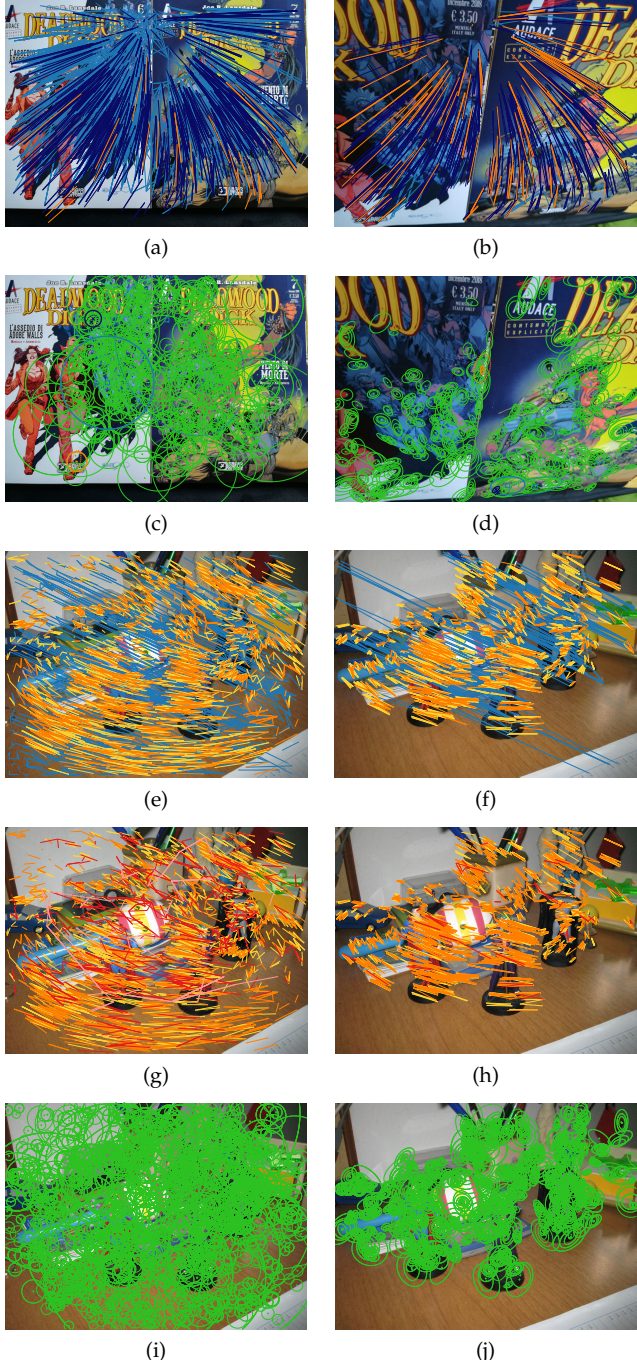


Fig. 12. Clusters of vector flows representing matches and keypoint support regions superimposed on planar and non-planar image pairs according to different ground-truth estimation methods when using SIFT (left column) and HarrisZ (right column). (first row) Method B (blue and light blue), method C (blue) and method D (blue and orange). (second row) Descriptor support regions for each keypoint match found in the previous row. The worst matches according to the reprojection error for each colored cluster are evidenced, the dashed ellipses are reprojected from the other image and the overlap error is computed by doubling the shape size. (third row) Method A (light blue and yellow) by setting the epipolar line error distance threshold to 7 pixels and method D (yellow and orange). (fourth row) Method B (yellow, red and light red), C (yellow and red) and D (yellow and orange). (fifth row) Descriptor support regions for each correspondence found by methods C and D (see Sec. 5.1, best viewed in color and zoomed in).

## APPENDIX D

### DTM EVALUATION

Tables 1-3 report the results of the local spatial filters evaluation for planar and non-planar scenes, without or with 1SAC applied as post-processing. The following statistics, averaged on the image pairs, are included: The precision, the recall, the number of correct and output matches, the number failures (i.e. the number of times the method did not provide at least one ground-truth match), and the running time.

TABLE 1

Local spatial filter results global statistics. The average planar/non-planar number of ground-truth matches per image pair are 551/429 (blob  $\cup$  OANet, for recall), 963/691 (all matches, for recall\*)

		precision (%)	recall (%)	recall* (%)	correct matches	output matches	failures	time (s)
no model	blob	29.29	99.23	55.83	548	4091	0	–
	th	90.74	50.16	30.28	310	408	1	0.000
	DTM <sub>1</sub>	81.92	66.37	39.65	419	844	0	0.590
	DTM <sub>2</sub>	82.78	75.13	44.21	461	907	0	1.186
	LMR	80.47	64.26	37.47	396	598	1	0.127
	LPM	78.32	49.48	28.24	307	447	2	0.030
	GLPM	80.34	65.08	39.18	413	760	4	0.057
	GMS	73.06	35.85	23.37	292	599	18	0.644
	VFC	82.06	88.09	51.03	520	1134	3	0.044
	LLT	48.02	54.23	32.84	352	1061	27	3.325
planar	OANet	89.03	44.55	24.65	253	343	0	1.278
	blob	90.27	71.85	43.17	446	729	5	–
	th	89.80	43.75	27.03	285	352	7	–
	DTM <sub>1</sub>	89.91	52.54	32.54	357	574	7	–
	DTM <sub>2</sub>	90.86	59.40	36.27	392	619	6	–
	LMR	91.91	55.02	32.80	354	475	6	–
	LPM	88.87	42.28	24.63	273	352	8	–
	GLPM	91.21	56.55	34.42	368	556	6	–
	GMS	73.83	32.49	21.31	266	462	19	–
	VFC	91.76	72.46	43.17	451	735	5	–
ISAC	LLT	61.31	43.91	27.33	298	473	28	–
	OANet	88.87	34.06	19.14	195	237	4	–
	blob	21.59	98.26	59.13	424	4107	0	–
	th	77.66	36.19	23.25	173	253	1	0.000
	DTM <sub>1</sub>	65.48	63.03	40.04	298	737	1	0.558
	DTM <sub>2</sub>	65.42	69.80	43.82	326	789	0	1.153
	LMR	67.26	57.49	34.72	260	463	1	0.128
	LPM	65.40	45.70	26.23	196	337	2	0.030
	GLPM	65.09	51.22	32.66	250	526	6	0.033
	GMS	72.56	39.18	26.71	224	516	11	0.605
non-planar	VFC	53.92	84.86	52.75	397	1305	4	0.049
	LLT	39.93	63.44	39.94	309	1280	23	3.197
	OANet	79.87	41.36	23.84	172	256	0	1.275
	blob	59.78	73.86	46.84	352	899	1	–
	th	84.58	32.32	21.10	158	210	3	–
	DTM <sub>1</sub>	78.86	53.34	34.64	263	509	2	–
	DTM <sub>2</sub>	78.77	58.70	37.72	286	544	2	–
	LMR	81.17	51.29	31.46	239	352	2	–
	LPM	78.61	41.04	23.87	181	258	4	–
	GLPM	76.86	46.85	30.05	232	396	7	–
ISAC	GMS	75.56	36.21	24.73	209	424	13	–
	VFC	69.62	72.18	45.67	349	764	4	–
	LLT	54.92	54.40	34.85	273	591	23	–
	OANet	79.91	35.62	20.80	151	213	0	–

The recall is computed with respect to the ground-truth matches of the specific pipelined blob matching, together with those provided by OANet. The tables also include recall\*, that considers the overall ground-truth matches among all the tested configurations. For the comparison, the former recall definition is more reasonable, since the local spatial filters cannot include matches outside those provided to them as input, i.e. the blob matching output.

TABLE 2

Local spatial filter results for the baseline configuration. The average planar/non-planar number of ground-truth matches per image pair are 367/257 (blob  $\cup$  OANet, for recall), 997/696 (all matches, for recall\*)

		precision (%)	recall (%)	recall* (%)	correct matches	output matches	failures	time (s)	
planar	no model	blob	21.77	97.15	33.96	360	1570	0	–
		th	82.28	35.48	14.11	161	172	2	0.000
		DTM <sub>1</sub>	77.22	54.63	20.87	251	275	0	0.329
		DTM <sub>2</sub>	79.14	66.09	24.90	288	316	0	0.530
		LMR	75.35	65.73	25.02	293	328	2	0.056
		LPM	72.78	63.43	24.36	296	333	6	0.013
		GLPM	78.90	53.66	21.95	266	282	9	0.021
		GMS	55.43	18.12	7.85	124	125	33	0.614
		VFC	79.36	79.54	29.30	326	347	6	0.022
		LLT	44.43	46.92	18.65	258	333	32	0.808
		OANet	82.22	51.58	18.91	210	297	0	1.271
ISAC	no model	blob	79.31	54.54	21.96	272	272	13	–
		th	76.63	27.20	11.52	146	146	17	–
		DTM <sub>1</sub>	75.81	38.56	15.86	209	210	17	–
		DTM <sub>2</sub>	79.50	45.96	18.71	238	239	14	–
		LMR	86.50	52.17	20.79	256	256	9	–
		LPM	83.84	50.50	20.17	256	257	10	–
		GLPM	81.36	46.68	19.28	238	238	13	–
		GMS	53.32	16.85	7.34	116	116	35	–
		VFC	87.04	61.71	23.85	279	280	8	–
		LLT	55.86	37.31	15.10	217	218	32	–
		OANet	81.96	38.75	14.99	178	222	7	–
non-planar	no model	blob	16.05	94.00	32.78	244	1593	0	–
		th	67.03	27.12	11.02	84	108	2	0.000
		DTM <sub>1</sub>	61.47	54.12	20.58	159	224	1	0.331
		DTM <sub>2</sub>	61.33	62.94	23.67	182	260	1	0.538
		LMR	61.65	62.51	23.57	182	256	2	0.058
		LPM	61.88	61.96	23.77	187	264	2	0.013
		GLPM	66.65	43.44	18.03	147	183	10	0.014
		GMS	62.38	19.59	8.43	82	92	29	0.603
		VFC	49.51	78.86	29.30	229	407	6	0.030
		LLT	37.50	59.98	23.10	196	388	20	0.897
		OANet	71.53	52.16	18.64	140	236	0	1.288
ISAC	no model	blob	52.42	64.47	25.32	198	309	4	–
		th	77.37	23.83	10.07	78	86	6	–
		DTM <sub>1</sub>	73.81	45.02	18.08	142	165	6	–
		DTM <sub>2</sub>	74.19	51.64	20.53	161	189	5	–
		LMR	75.15	54.42	21.31	167	194	4	–
		LPM	74.43	55.23	21.71	172	202	5	–
		GLPM	71.16	40.28	17.01	139	156	16	–
		GMS	60.21	18.31	7.97	77	83	34	–
		VFC	64.74	65.71	25.46	203	265	6	–
		LLT	51.56	51.83	20.49	175	235	21	–
		OANet	71.58	44.35	16.37	124	193	0	–

Nevertheless recall\* can give clues of the whole pipeline performances.

Figures 13-14 provide a visual qualitative analysis of the local spatial filters evaluated in Sec. 5.3. VFC is very effective in the presence of large planar structures (DD15, Spidey13 and Kampa) but in the other cases it may leave in many outliers (LeuvenB and Fountain01). OANet is quite accurate but can leave out many inliers (Spidey13, Horse and Valbonne) especially in the presence of repeated patterns (NapierB). GMS does not work well when consistent clusters of outliers are predominant (LeuvenB, Fountain01). Simple threshold th is

TABLE 3

Local spatial filter results for the best configuration. The average planar/non-planar number of ground-truth matches per image pair are 681/575 (blob  $\cup$  OANet, for recall), 928/686 (all matches, for recall\*)

		precision (%)	recall (%)	recall* (%)	correct matches	output matches	failures	time (s)	
planar	no model	blob	32.79	99.87	73.48	680	6104	0	–
		th	98.75	63.74	48.35	466	769	0	0.000
		DTM <sub>1</sub>	87.38	77.42	58.22	561	1528	0	0.879
		DTM <sub>2</sub>	87.90	83.49	62.40	598	1610	0	1.820
		LMR	89.22	64.52	48.13	474	933	0	0.186
		LPM	89.16	40.12	30.91	313	696	0	0.044
		GLPM	87.77	76.68	57.84	559	1539	0	0.119
		GMS	84.25	54.60	42.47	463	1351	9	0.662
		VFC	90.70	93.52	69.79	663	1898	2	0.046
		LLT	57.27	59.07	45.26	378	1383	23	6.751
		OANet	92.69	37.83	27.42	275	365	0	1.354
ISAC	no model	blob	98.46	88.02	65.37	613	1539	1	–
		th	98.58	60.45	45.86	445	724	1	–
		DTM <sub>1</sub>	98.53	69.46	52.54	515	1220	1	–
		DTM <sub>2</sub>	98.54	74.79	56.26	547	1285	1	–
		LMR	96.83	56.93	42.87	431	798	2	–
		LPM	95.09	35.93	27.84	288	600	3	–
		GLPM	98.52	70.23	53.17	517	1234	1	–
		GMS	87.57	49.96	39.04	426	1090	9	–
		VFC	96.52	84.40	63.34	607	1523	2	–
		LLT	69.15	53.42	41.09	342	883	23	–
		OANet	91.51	28.50	20.73	191	229	4	–
non-planar	no model	blob	24.03	99.55	81.56	573	5955	0	–
		th	90.16	41.87	35.90	261	424	0	0.000
		DTM <sub>1</sub>	70.00	70.90	59.39	432	1293	0	0.773
		DTM <sub>2</sub>	70.05	75.03	62.73	455	1351	0	1.658
		LMR	74.91	53.09	44.49	328	697	0	0.181
		LPM	73.62	29.68	25.21	181	451	0	0.043
		GLPM	69.67	55.42	47.21	348	1001	3	0.061
		GMS	75.72	57.09	48.45	379	1135	6	0.592
		VFC	58.14	87.11	72.87	537	2069	3	0.055
		LLT	41.77	56.84	48.51	366	1616	23	5.751
		OANet	88.25	35.08	28.69	202	274	0	1.264
ISAC	no model	blob	66.79	82.19	68.63	498	1629	0	–
		th	92.91	38.10	32.73	238	378	1	–
		DTM <sub>1</sub>	85.37	61.87	52.34	387	978	1	–
		DTM <sub>2</sub>	85.11	65.16	55.07	407	1020	0	–
		LMR	88.26	48.01	40.60	304	565	0	–
		LPM	85.12	27.11	23.21	168	373	3	–
		GLPM	84.06	49.87	42.64	315	775	3	–
		GMS	81.96	50.68	43.23	338	914	6	–
		VFC	75.33	75.32	63.47	474	1358	3	–
		LLT	59.59	51.86	44.44	336	982	23	–
		OANet	88.07	29.86	24.59	175	227	0	–

in general adequate, but can leave out many inliers, decreasing successive model estimation accuracy (Bf, Valbonne and Horse). LPM, LMR and DTM increasingly include more inliers and thus improve the recall, maintaining a low number of outliers. DTM results are the most balanced overall. GLPM and LLT results are not reported due to lack of space. Nevertheless, GLPM results dangle between those of LPM and th, while LLT has in general a high number of outliers.

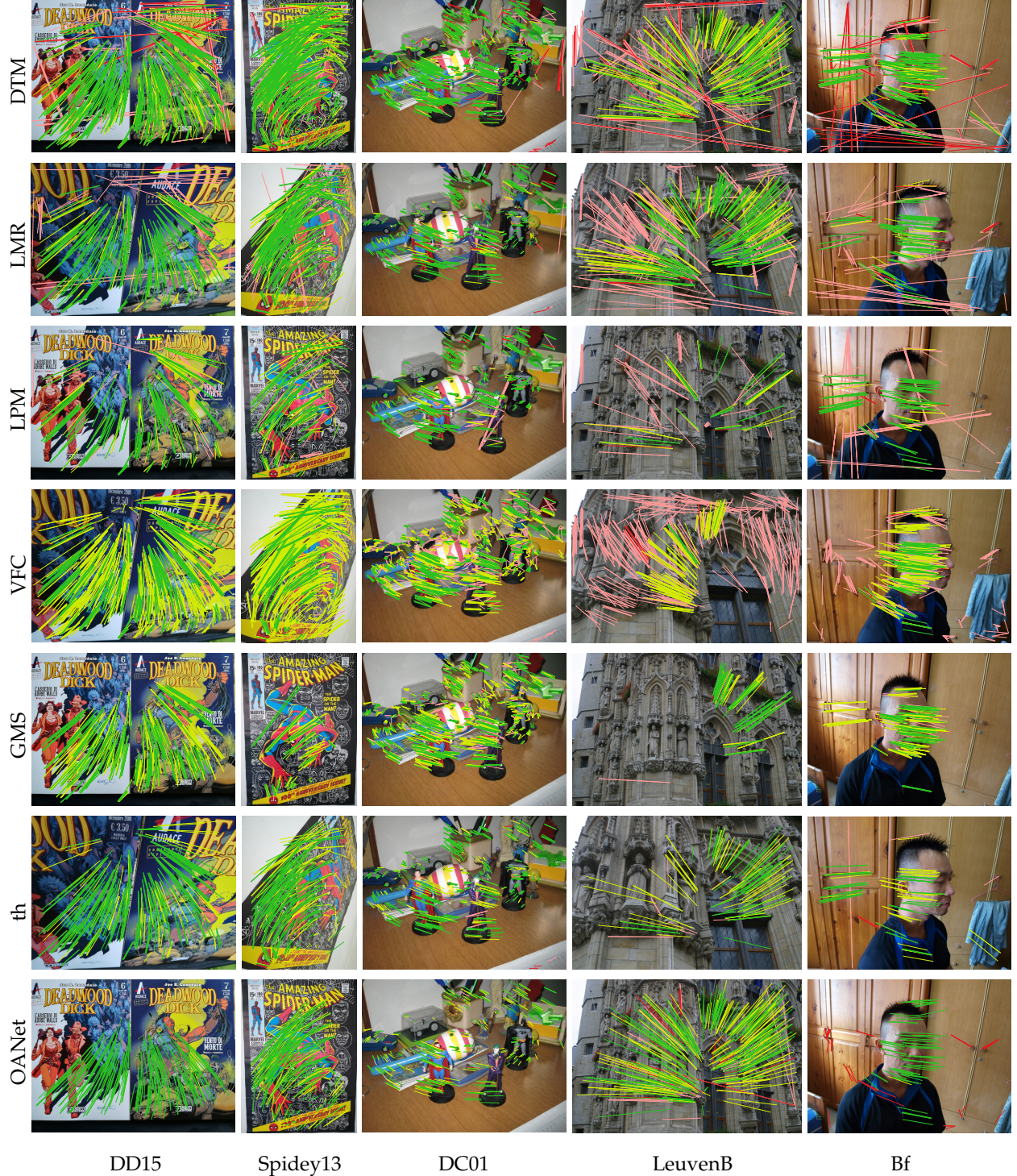


Fig. 13. Planar and non-planar local spatial filter results according to the best configuration setup, the image of the input pair alternate among the rows. Image indexes are reported as suffix when the sequence contains more than two images. For each method inlier (yellow, green) and outlier (red and light red) clusters are shown, as well as the 1SAC filtered results (green, red) (see Sec. 5.3, best viewed in color and zoomed in).

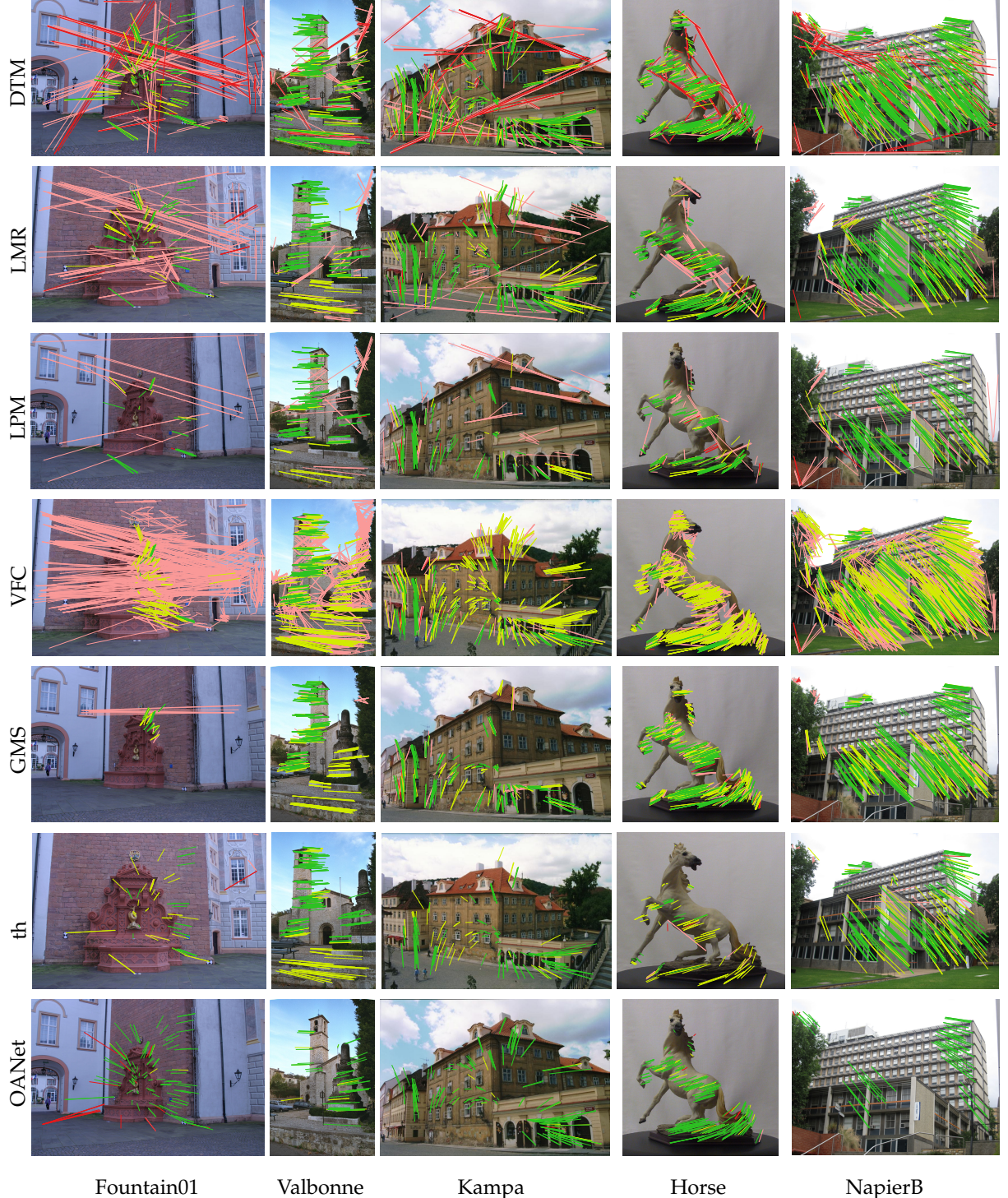


Fig. 14. Non-planar local spatial filter results according to the best configuration setup, the image of the input pair alternate among the rows. Image indexes are reported as suffix when the sequence contains more than two images. For each method inlier (yellow, green) and outlier (red and light red) clusters are shown, as well as the 1SAC filtered results (green, red) (see Sec. 5.3, best viewed in color and zoomed in).